

Low-resolution simulations of vesicle suspensions in 2D

Gökberk Kabacaoğlu^a, Bryan Quaife^b, George Biros^c

^aDepartment of Mechanical Engineering,
The University of Texas at Austin, Austin, TX, 78712, United States

^bDepartment of Scientific Computing,
Florida State University, Tallahassee, FL 32306, United States

^cInstitute for Computational Engineering and Sciences,
The University of Texas at Austin, Austin, TX, 78712, United States

Abstract

We develop a robust method for simulating vesicle suspensions in a two-dimensional Stokesian fluid at low discretization resolutions. This method is an extension of our previous work [42, 44]. Vesicle suspensions model biological systems such as microcirculation, where the blood flow is dictated by red blood cells. Vesicle flows are characterized by rich and complex dynamics of vesicles due to their large deformations and nonlinear elastic properties. Additionally, vesicles can become arbitrarily close to each other but they never collide due to the lubrication forces in the fluid between two vesicles. It requires sufficient spatial and temporal resolutions to capture highly deforming membranes and vesicle-vesicle interactions accurately. However, high-resolution simulations are prohibitively expensive.

We present low-resolution correction algorithms (LRCA) for stably and accurately simulating vesicle suspensions at low resolutions. These algorithms include anti-aliasing to compute the nonlinear terms without introducing spurious oscillations, adaptive time stepping, membrane reparametrization, correction of vesicles' area and arc-length, and a repulsion force for handling vesicle collisions. We, then, perform a systematic error analysis by comparing the low-resolution simulations of dilute and dense suspensions with their high-fidelity counterparts. We observe that the LRCA enable both efficient and statistically accurate low-resolution simulations of vesicle suspensions.

Key words: Particulate flows, Suspensions, Stokes flow, Vesicle suspensions, Red blood cells

1. Introduction

Vesicle suspensions are deformable capsules filled with and submerged in an incompressible fluid. Their simulation plays an important role in many biological applications [25, 48], such as biomembranes [47] and red blood cells [15, 23, 31, 34, 40]. Here we discuss algorithms for simulating the motion of vesicles suspended in two-dimensional Stokesian fluids. In particular, we focus on algorithms that enable stable and statistically accurate simulations at low resolutions. Vesicle flows are characterized by large deformations, the local inextensibility of a vesicle's membrane, the conservation of enclosed area due to the incompressibility of the fluid inside the vesicle, and the stiffness related to tension and bending forces. These characteristics make suspensions at low resolutions a challenging problem.

In line with our previous work [42, 43, 45, 49, 50], and work of others [13, 14, 30, 46, 52–55], we use an integral equation formulation for the viscous interfacial flow [41]. Our previous results for simulating high-concentration vesicle suspensions in two dimensions [42, 43] focus on accurate quadrature and high-order semi-implicit time stepping. The results in those papers assume sufficient resolution and provide a robust framework for simulations. For example, vesicles do not collide because all hydrodynamic interactions

Email addresses: gokberk@ices.utexas.edu (Gökberk Kabacaoğlu), bquaife@fsu.edu (Bryan Quaife), gbiros@acm.org (George Biros)

are resolved with spectral accuracy. Thus, there is no need to introduce artificial repulsion forces between vesicles. We can accurately resolve long time horizon, concentrated suspensions with roughly 96 or 128 points per vesicle. But in three dimensions such a resolution is prohibitively expensive. For example, a similar resolution using the 3D version of these algorithms [29] would require over 10,000 points per vesicle. Therefore, there is a need to develop numerical algorithms that maintain stability in simulations, all the while accurately capturing the statistics of the underlying flow using as coarse discretization as possible. To measure the accuracy of the statistics, we develop the algorithms in two dimensions so that we can compare with “ground truth” simulations performed at an adequate resolution. Demonstrating the effectiveness of these algorithms at low resolutions is the first step towards extending them to three dimensions.

Contributions. In this paper, we continue our efforts towards efficient and stable algorithms for simulating two-dimensional vesicle flows using an integral equation formulation. Low-resolution simulations of vesicle suspensions can become unstable as a result of spurious oscillations in vesicles’ shapes due to computing nonlinear terms, non-physical changes in vesicles’ areas and arc-lengths, and vesicle collisions. We address these issues and develop a robust method by implementing some standard techniques and also introducing new schemes. The parameters for these algorithms are calibrated by carefully comparing low resolution simulations that use our low-resolution correction algorithms (LRCA) with high-fidelity solutions. In this we are able to minimize the effect of the LRCA on the underlying physics. Additionally, we investigate accuracy of our low-resolution simulations. We summarize these contributions as follows:

- We introduce an efficient algorithm for determining an upsampling rate that is sufficient for controlling the aliasing errors caused by nonlinear terms, but not too large so that the computational costs are not unnecessarily inflated. Additionally, we formulate the reparametrization algorithm in [50] to two dimensions.
- Our previous adaptive time stepping work [44] relied on asymptotic assumptions of the truncation error which are not valid at the low resolutions. Since this result breaks down, we present a new variation of this scheme which can be used at all resolutions.
- A vesicle’s area and arc-length are invariant in two-dimensional vesicle simulations. However, at low resolutions the errors can be extensive and hence result in unstable and non-physical flows in time scales much shorter than the target time horizons. Therefore, we present an efficient scheme to correct those errors without modifying the governing equations.
- The hydrodynamic interactions cannot be resolved accurately at low resolutions. This leads to non-physical collisions between vesicles. We detect collisions with spectral accuracy [42] and implement a short range repulsion force [19, 51] to keep vesicles sufficiently separated.
- We discuss new error measures and perform a systematic error analysis to investigate the accuracy of our low-resolution simulations.

Limitations. One limitation is that our results are entirely empirical. In general, there is very little work on theoretical results for general vesicles. Indeed the only results are for vesicles that are small perturbations of a disc and thus resemble rigid spheres. Another limitation is that the methods are implemented in two dimensions. However, the algorithms can be naturally extended to three dimensions which we leave as future work. For instance, local area and length correction can be extended to a volume and surface area correction [29], and a surface reparameterization has already been implemented in three dimensions [29, 46, 50]. Another limitation is that our methods do not allow for spatial adaptivity. However, upsampling is utilized to avoid aliasing that would otherwise be unavoidable at low frequencies.

Our methods allow for a viscosity contrast between the interior and exterior of the vesicles, and several numerical examples are presented. But the methods are not directly applicable to suspensions in which the bulk fluid is non-Newtonian or inertial flows.

Related work. This paper is an extension of our work for high-concentration suspensions [42] and for high-order adaptive time stepping with spectral deferred correction (SDC) [44]. Here, we only review the literature on anti-aliasing techniques, surface reparametrization algorithms, area-length correction methods, repulsion models, and error measures for vesicle dynamics and rheology.

Anti-aliasing. Classical works in aliasing include [9, 26, 38]. In [35] and [36], the nonlinear terms are computed at the higher resolution $M = 1.5N$ and filtered back to N points. While this removes aliasing errors due to quadratic operations, the nonlinearities in the vesicle model, such as roots and inverses, are much stronger. Therefore, it is essential to find appropriate upsampling rates. In [46], an algorithm that automatically adjusts the upsampling rate for differentiation is based on the mean curvature of the three-dimensional vesicles; our upsampling scheme is similar. It efficiently determines the sufficient upsampling rate for each vesicle to compute the force due to bending while we always upsample to $N^{3/2}$ to compute the layer potentials.

Reparametrization. By using reparametrization, the grid quality of the vesicle membrane is preserved and this also helps control aliasing errors. An algorithm for distributing grid points equally in arc-length for two-dimensional membranes is presented in [5] and implemented in [20, 30]. Additionally, [46, 50] present a reparametrization scheme for three-dimensional vesicles which redistributes points so that high-frequency components of the spectral discretization are minimized. Our reparametrization scheme is based on these works. It smooths vesicle shapes by penalizing its high frequency components.

Local correction to area and arc-length. Despite the local inextensibility and incompressibility conditions, errors in the area and length of a vesicle can become large because of error accumulating at each time step. This not only results in non-physical vesicle shapes, but can also lead to instabilities. In [30], this issue is addressed by performing an area-length correction after each time step. The length is corrected by adding a correction term to the inextensibility condition and the area correction requires solving a quadratic equation. In [1, 6, 8], area and length errors are corrected by adding artificial forces. Unlike those techniques, our area-length correction scheme does not change the governing equations. We correct area and length after each time step by solving a constrained optimization problem. This scheme is also extended to three-dimensions in [29].

Repulsion. There is extensive work on repulsion force models for avoiding collisions in particulate flows [11, 12, 16, 37]. The models in these studies have two parameters. One is the length scale where the force is non-zero and the other is the strength of the force. These models are in either polynomial or exponential form. Here, we implement the repulsion force model introduced in the context of contact mechanics [19, 51], which have not been used in vesicle flows before. This model is in a polynomial form which works well for dense suspension simulations because it is developed for simulations with objects coming close frequently with low velocities. We calibrate the parameters of this repulsion force by comparing its effect on a low-resolution simulation with a high-resolution simulation.

Error measures. A significant question that arises in these low-resolution calculations is an appropriate definition of the error. Obviously one has to give up on capturing individual trajectories accurately and look at appropriate statistics that should depend on the particular application. Since we do not have a particular goal in mind and we consider this coarsening problem generically, it is useful to first quantify the error in individual trajectories so that we better understand the sources of error. But of course, eventually we need to evaluate error in suspensions.

The dynamics and rheology of vesicle suspensions have been investigated widely and various error measures have been introduced. We mention some of the work that is most relevant to ours. In [22, 24, 27], the error is quantified using the vesicles' inclination angles and centers in dilute suspensions. In [45], the distance between two vesicles in a shear flow is computed. For dense suspensions, it is typical to consider collective dynamics rather than the behavior of each vesicle. For instance, effective viscosity of a suspension is an upscaling measure which is equivalent to the viscosity of a homogeneous Newtonian fluid having the same energy dissipation as the suspension. We might be interested in capturing the effective viscosity of a suspension [45]. Additionally, in [10, 28], the so-called shear-induced diffusion, that is, the evolution of probability distributions of vesicles' centers is investigated. This phenomenon is studied both computationally [32, 33] and experimentally [39]. We also studied mixing in vesicle suspension in [21],

where we need accurate averages of velocity field. In this study, we quantify the error based on those quantities of interest.

Outline of the paper. In Section 2 we summarize the formulation of our problem. In Section 3 we introduce the LRCA including anti-aliasing, a new adaptive time stepping method, area-length correction, reparametrization, repulsion and alignment of shapes. In Section 4 we test the stability of the low-resolution simulations with the LRCA in various confined and unconfined flows, and we report accuracies in terms of different error measures.

2. Formulation

In this section, we summarize the formulation and discretization algorithm from [42] (see [41] for a detailed derivation).

2.1. Governing equations

In the length and velocity scales of vesicle flows, the inertial forces are often negligible so we use the quasi-static incompressible Stokes equations. The dynamics of the flow is fully characterized by the position of the interface $\mathbf{x}(s, t) \in \gamma_i$, where s is arc-length, t is time, and γ_i is the membrane of the i^{th} vesicle. Given M vesicles, we define $\gamma = \bigcup_{i=1}^M \gamma_i$. The interior of the i^{th} vesicle is denoted by ω_i , and we define $\omega = \omega_1 \cup \dots \cup \omega_M$. Let Ω be the m -ply connected domain containing the vesicles, and $\Gamma = \Gamma_0 \cup \Gamma_1 \cup \dots \cup \Gamma_m$ be its boundary. The interior connected components of Γ are Γ_i , $i = 1, \dots, m$, and Γ_0 is the connected component containing all other connected components. See Figure 1 for the schematic.

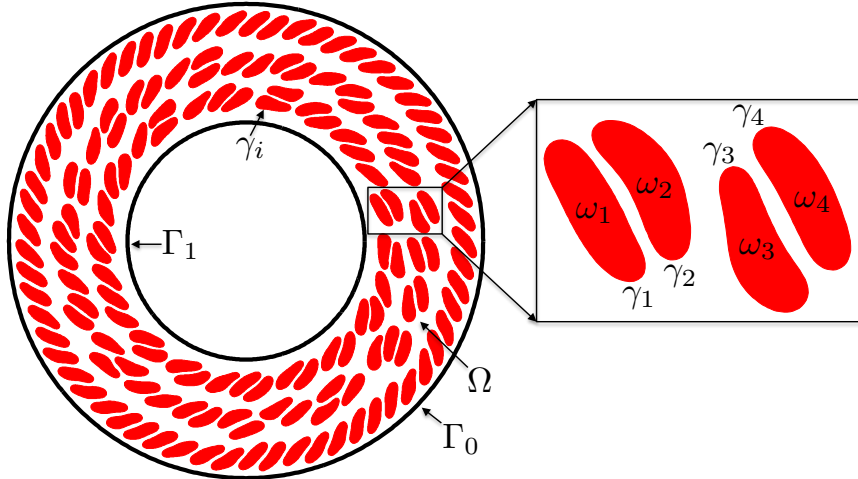


Figure 1: A vesicle suspension in a Couette apparatus. Ω is the fluid domain between the walls (both inside and outside the vesicles), its boundary is denoted by Γ , γ_i is the boundary of the i^{th} vesicle whose interior is ω_i , $\omega = \bigcup_i \omega_i$ is the red area, and $\gamma = \bigcup_i \gamma_i$.

Let μ and μ_i be the viscosities of the bulk fluid and the interior fluid of the i^{th} vesicle, respectively. The position of the vesicle is determined by the moving interface problem modeling the mechanical interactions between the viscous incompressible fluids and the vesicles' boundaries. The equations governing the

motion of vesicles are

$$\mu \nabla \cdot (\nabla \mathbf{u}(\mathbf{x}) + \nabla \mathbf{u}^T(\mathbf{x})) - \nabla p(\mathbf{x}) = 0, \quad \mathbf{x} \in \Omega \setminus \gamma, \text{ conservation of momentum,} \quad (1a)$$

$$\nabla \cdot \mathbf{u}(\mathbf{x}) = 0, \quad \mathbf{x} \in \Omega \setminus \gamma, \quad \text{conservation of mass,} \quad (1b)$$

$$\mathbf{x}_s \cdot \mathbf{u}_s = 0, \quad \mathbf{x} \in \gamma, \quad \text{vesicle inextensibility,} \quad (1c)$$

$$\mathbf{u}(\mathbf{x}, t) = \dot{\mathbf{x}}(t), \quad \mathbf{x} \in \gamma, \quad \text{velocity continuity,} \quad (1d)$$

$$-\kappa_b \mathbf{x}_{ssss} + (\sigma(\mathbf{x}) \mathbf{x}_s)_s = \llbracket T \mathbf{n} \rrbracket, \quad \mathbf{x} \in \gamma, \quad \text{traction jump,} \quad (1e)$$

$$\mathbf{u}(\mathbf{x}, t) = \mathbf{U}(\mathbf{x}, t), \quad \mathbf{x} \in \Gamma, \quad \text{no-slip boundary condition.} \quad (1f)$$

Here $T = -pI + \mu (\nabla \mathbf{u} + \nabla \mathbf{u}^T)$ is the Cauchy stress tensor and \mathbf{n} is the outward normal vector to the membrane γ at point \mathbf{x} . $\llbracket \cdot \rrbracket$ denotes the jump across the interface, \mathbf{x}_s is arc-length derivative of \mathbf{x} , κ_b is bending stiffness of a membrane, and σ is tension of a membrane. Here, the right-hand side of (1e) is the interfacial force applied by the membrane to the fluid due to bending and tension. \mathbf{U} is velocity on the boundary Γ .

There exist several methods for solving interface evolution equations similar to (1). In line with our previous work [42–45, 49, 50], we use an integral equation formulation which naturally handle the piecewise constant viscosity and the discontinuity along the interface.

2.2. Integral equation formulation

We present an integral equation formulation of (1) with a viscosity contrast $\nu_p = \mu_p/\mu$ between the interior fluid with viscosity μ_p and the exterior fluid with viscosity μ . The single and double layer potentials for Stokes flow (\mathcal{S}_{pq} and \mathcal{D}_{pq} , respectively) denote the potential induced by hydrodynamic densities of the interfacial force \mathbf{f} and velocity \mathbf{u} on vesicle q and evaluated on vesicle p :

$$\mathcal{S}_{pq}[\mathbf{f}](\mathbf{x}) := \frac{1}{4\pi\mu} \int_{\gamma_q} \left(-\mathbf{I} \log \rho + \frac{\mathbf{r} \otimes \mathbf{r}}{\rho^2} \right) \mathbf{f}(\mathbf{y}) ds_{\mathbf{y}}, \quad \mathbf{x} \in \gamma_p, \quad (2a)$$

$$\mathcal{D}_{pq}[\mathbf{u}](\mathbf{x}) := \frac{1 - \nu_q}{\pi} \int_{\gamma_q} \frac{\mathbf{r} \cdot \mathbf{n}}{\rho^2} \frac{\mathbf{r} \otimes \mathbf{r}}{\rho^2} \mathbf{u}(\mathbf{y}) ds_{\mathbf{y}}, \quad \mathbf{x} \in \gamma_p, \quad (2b)$$

where $\mathbf{r} = \mathbf{x} - \mathbf{y}$ and $\rho = \|\mathbf{r}\|_2$. Let $\mathcal{S}_p := \mathcal{S}_{pp}$ and $\mathcal{D}_p := \mathcal{D}_{pp}$ denote vesicle self-interactions. We, then, define

$$\mathcal{E}_{pq}[\mathbf{f}, \mathbf{u}](\mathbf{x}) = \mathcal{S}_{pq}[\mathbf{f}](\mathbf{x}) + \mathcal{D}_{pq}[\mathbf{u}](\mathbf{x}), \quad \mathbf{x} \in \gamma_p,$$

$$\mathcal{E}_p[\mathbf{f}, \mathbf{u}](\mathbf{x}) = \sum_{q=1}^M \mathcal{E}_{pq}[\mathbf{f}, \mathbf{u}](\mathbf{x}), \quad \mathbf{x} \in \gamma_p.$$

For confined flows, we use the completed double layer potential due to a density function $\boldsymbol{\eta}$ defined on the solid walls

$$\mathcal{B}[\boldsymbol{\eta}](\mathbf{x}) = \mathcal{D}_{\Gamma}[\boldsymbol{\eta}](\mathbf{x}) + \sum_{q=1}^M R[\xi_q(\boldsymbol{\eta}), \mathbf{c}_q](\mathbf{x}) + \sum_{q=1}^M S[\boldsymbol{\lambda}_q(\boldsymbol{\eta}), \mathbf{c}_q](\mathbf{x}), \quad \mathbf{x} \in \gamma \cup \Gamma.$$

The Stokeslets and rotlets are

$$S[\boldsymbol{\lambda}_q(\boldsymbol{\eta}), \mathbf{c}_q](\mathbf{x}) = \frac{1}{4\pi\mu} \left(-\log \rho + \frac{\mathbf{r} \otimes \mathbf{r}}{\rho^2} \right) \boldsymbol{\lambda}_q(\boldsymbol{\eta}) \quad \text{and} \quad R[\xi_q(\boldsymbol{\eta}), \mathbf{c}_q](\mathbf{x}) = \frac{\xi_q(\boldsymbol{\eta})}{\mu} \frac{\mathbf{r}^\perp}{\rho^2},$$

where \mathbf{c}_q is a point inside ω_q , $\mathbf{r} = \mathbf{x} - \mathbf{c}_q$, and $\mathbf{r}^\perp = (r_2, -r_1)$. The size of the Stokeslets and rotlets are

$$\boldsymbol{\lambda}_{q,i} = \frac{1}{2\pi} \int_{\gamma_q} \boldsymbol{\eta}_i(\mathbf{y}) ds_{\mathbf{y}}, \quad i = 1, 2 \quad \text{and} \quad \xi_q = \frac{1}{2\pi} \int_{\gamma_q} \mathbf{y}^\perp \cdot \boldsymbol{\eta}(\mathbf{y}) ds_{\mathbf{y}}.$$

If $\mathbf{x} \in \Gamma_0$, we add the rank one modification $\mathcal{N}_0[\boldsymbol{\eta}](\mathbf{x}) = \int_{\Gamma_0} (\mathbf{n}(\mathbf{x}) \otimes \mathbf{n}(\mathbf{y})) \boldsymbol{\eta}(\mathbf{y}) d\mathbf{s}_y$ to \mathcal{B} to remove a one-dimensional null space. Finally, by expressing the inextensibility constraint in operator form as

$$\mathcal{P}[\mathbf{u}](\mathbf{x}) = \mathbf{x}_s \cdot \mathbf{u}_s,$$

the integral equation formulation of (1) is

$$(1 + \nu_p) \mathbf{u}(\mathbf{x}) = \mathcal{E}_p[\mathbf{f}, \mathbf{u}](\mathbf{x}) + \mathcal{B}_p[\boldsymbol{\eta}](\mathbf{x}), \quad \mathbf{x} \in \gamma_p, \quad \text{vesicle evolution}, \quad (3a)$$

$$(1 + \nu_p) \mathbf{U}(\mathbf{x}) = -\frac{1}{2} \boldsymbol{\eta}(\mathbf{x}) + \mathcal{E}_\Gamma[\mathbf{f}, \mathbf{u}](\mathbf{x}) + \mathcal{B}[\boldsymbol{\eta}](\mathbf{x}), \quad \mathbf{x} \in \Gamma, \quad \text{fixed boundaries}, \quad (3b)$$

$$\mathcal{P}[\mathbf{u}](\mathbf{x}) = 0, \quad \mathbf{x} \in \gamma_p, \quad \text{vesicle inextensibility}. \quad (3c)$$

Since the velocity $\mathbf{u} = d\mathbf{x}/dt$ and the interfacial force \mathbf{f} depend on σ and \mathbf{x} , (3) is a system of integro-differential-algebraic equations for \mathbf{x} , σ , and $\boldsymbol{\eta}$.

2.3. Temporal discretization

We discretize (3) in time with a first-order IMEX [4] time stepping method. We linearize (3) and treat the stiff terms, such as the bending, implicitly, while treating nonlinear terms, such as the layer potential kernel, explicitly. In particular, an approximation for the position \mathbf{x} and tension σ of vesicle p at time $n + 1$ is computed by solving

$$\frac{\alpha_p}{\Delta t} (\mathbf{x}_p^{n+1} - \mathbf{x}_p^n) = \mathcal{S}_p^n \mathbf{f}_p^{n+1} + \mathcal{D}_p^n \mathbf{u}_p^{n+1} + \mathcal{B}_p[\boldsymbol{\eta}^{n+1}] + \sum_{\substack{q=1 \\ q \neq p}}^M \mathcal{E}_{pq}^n [\mathbf{f}_q^{n+1}, \mathbf{u}_q^{n+1}], \quad \mathbf{x} \in \gamma_p \quad (4a)$$

$$\mathbf{U}^{n+1}(\mathbf{x}) = -\frac{1}{2} \boldsymbol{\eta}^{n+1}(\mathbf{x}) + \mathcal{E}_\Gamma^n [\mathbf{f}^{n+1}, \mathbf{u}^{n+1}](\mathbf{x}) + \mathcal{B}[\boldsymbol{\eta}^{n+1}](\mathbf{x}) + \mathcal{N}_0[\boldsymbol{\eta}^{n+1}](\mathbf{x}), \quad \mathbf{x} \in \Gamma, \quad (4b)$$

$$\mathcal{P}^n \mathbf{x}_p^{n+1} = \mathcal{P}^n \mathbf{x}_p^n, \quad \mathbf{x} \in \gamma_p, \quad (4c)$$

$$\mathbf{u}_p^{n+1} = \frac{\mathbf{x}_p^{n+1} - \mathbf{x}_p^n}{\Delta t}, \quad \mathbf{x} \in \gamma_p, \quad (4d)$$

where $\alpha_p = (1 + \nu_p)/2$, and operators with a superscript n are discretized at \mathbf{x}^n . Although (4) is fully coupled, it is more stable method than methods that treat vesicle-vesicle and vesicle-boundary interactions explicitly [42]. In [44], we introduce new higher-order adaptive time integrators based on spectral deferred corrections (SDC). But as we will see, SDC is not stable enough for these low-resolution runs.

2.4. Spatial discretization

Let $\mathbf{x}(\theta)$, $\theta \in (0, 2\pi]$ be a parametrization of the interface γ_p , and let $\{\mathbf{x}(\theta_k) = 2k\pi/N\}_{k=1}^N$ be N uniformly distributed discretization points. Then, a spectral representation of the vesicle membrane is given by

$$\mathbf{x}(\theta) = \sum_{k=-N/2+1}^{N/2} \hat{\mathbf{x}}(k) e^{ik\theta}.$$

We use the fast Fourier transform to compute $\hat{\mathbf{x}}$, and arc-length derivatives are computed pseudospectrally. Nearly singular integrals are computed with an interpolation scheme [42]. Finally, we use a Gauss-trapezoid quadrature rule [2] with accuracy $\mathcal{O}(h^8 \log h)$ to evaluate the single layer potential and the spectrally accurate trapezoid rule for the double layer potential.

We build and factorize a block-diagonal preconditioner introduced in [42]. This preconditioner removes the stiffness due to the self-interactions of vesicles but does nothing for the inter-vesicle and inter-wall interactions. As a result, the number of preconditioned GMRES iterations depends mostly on the magnitude of the inter-vesicle interactions which is a function of the vesicles' proximity. As we will see later, we upsample vesicles' boundaries to avoid aliasing. Thus, we construct the preconditioner on the upsampled grid. Although this increases the cost of building the preconditioner, the cost is offset by a significant reduction in the number of GMRES iterations.

3. Algorithms for low-resolution simulations

In this section, we present our low-resolution correction algorithms (LRCA) for simulations of vesicle suspensions: anti-aliasing in Section 3.1, adaptive time stepping in Section 3.2, local correction to area and length in Section 3.3, reparametrization in Section 3.4, alignment of shapes in Section 3.5, and repulsion force in Section 3.6. In Algorithm 1, we list the order that these algorithms are called in conjunction with the advancing the vesicles forward one time step.

Algorithm 1 Main stages in one time step of vesicle flows

$[\mathbf{x}_{n+1}, \sigma_{n+1}, \boldsymbol{\eta}_{n+1}] = \text{timeStep}(\mathbf{x}_n, \sigma_n, \boldsymbol{\eta}_n, \Delta t_n)$	Solve the system of equations (4)
$[\text{accept}, \Delta t_{\text{new}}] = \text{newTimeStepSize}(\mathbf{x}_{n+1}, \mathbf{x}_n, \Delta t_n)$	Choose the new time step size
if accept then	If solution is accepted
$\tilde{\mathbf{x}}_{n+1} = \text{correctShape}(\mathbf{x}_{n+1}, A_0, L_0)$	Correct errors in area and length of vesicles
$\mathbf{x}_{n+1} = \text{alignShape}(\tilde{\mathbf{x}}_{n+1}, \mathbf{x}_{n+1})$	Align corrected shapes with the original ones
$\tilde{\mathbf{x}}_{n+1} = \text{reparametrize}(\mathbf{x}_{n+1})$	Reparametrize vesicles' membranes
$\mathbf{x}_{n+1} = \text{alignShape}(\tilde{\mathbf{x}}_{n+1}, \mathbf{x}_{n+1})$	Align reparametrized shapes with the original ones
$t = t + \Delta t_n$	
$\Delta t_{n+1} = \Delta t_{\text{new}}$	Set the time step size for the next time step
else	If solution is not accepted
$[\mathbf{x}_{n+1}, \sigma_{n+1}, \boldsymbol{\eta}_{n+1}] \leftarrow [\mathbf{x}_n, \sigma_n, \boldsymbol{\eta}_n]$	Reject solution and try again with smaller time step
$\Delta t_n = \Delta t_{\text{new}}$	Set the new time step size for the subsequent attempt
end if	

At every time step, we solve (4) with our anti-aliasing algorithm to update the vesicles' position \mathbf{x} , tension σ , and density function $\boldsymbol{\eta}$ (if the flow is confined). After solving the evolution equation, `newTimeStepSize` determines if the solution \mathbf{x}_{n+1} is accepted or rejected, and chooses a new time step size, Δt_{new} . If the solution \mathbf{x}_{n+1} is accepted, we correct the errors in area and length of every vesicle. We, then, reparametrize the vesicles' boundaries to redistribute points such that high frequency components of the surface parametrization are minimized. The reparametrization and the area-length correction cause vesicles to translate and rotate, so we align their centers and inclination angles with those of the original ones. Finally, if we detect that too much error has been committed, then the solution \mathbf{x}_{n+1} is rejected and a time step is taken with a smaller time step size.

We list and comment on the parameters required by the algorithms under the pertinent sections. Spatial resolution of a simulation is determined by numbers of points per vesicle N and per wall N_{wall} . The tolerance for the error in area and length at each time step, ρ_{AL} , sets the temporal resolution. Finally, the number of SDC sweeps n_{sdc} determines the time stepping order of accuracy. At low resolutions, we have observed that SDC does not achieve high-order accuracy unless a very small time step is taken meaning that a small tolerance ρ_{AL} is requested. Since we are not interested in taking small time step sizes, we do not use SDC sweeps for low-resolution simulations, but they are used for our ground truth high-resolution simulations.

3.1. Anti-aliasing

When representing periodic functions at N grid points, only N frequencies can be represented. Therefore, if a certain operation such as the multiplication of two periodic functions is performed, new high-frequency components are formed and can not be represented with N points. These newly introduced high-frequency components are identical to one of the low-frequency components, and the result is that the high-frequency components are aliased as one of the N frequencies.

In vesicle suspensions, two operations that result in aliasing errors, especially at low resolutions, are computing the traction jump $-\kappa_b \mathbf{x}_{ssss} + (\sigma \mathbf{x}_s)_s$, and computing the single and double layer potentials (2). The bending term \mathbf{x}_{ssss} is especially susceptible to aliasing errors since it requires multiplication by the Jacobian four times. We control the aliasing error by upsampling (uniformly). But how much should we upsample? We adjust the upsampling rate using the decay of the spectrum of \mathbf{x}_{ssss} . First, we upsample

the N point vesicle to $16N$ points and compute the fourth derivative of this upsampled shape. Then, we systematically compare the high-frequency and low-frequency energy using a growing number of points of this upsampled shape. We start by considering the first $1.5N$ Fourier modes. If the low-frequency energy exceeds the high-frequency energy, then we use 1.5 as the upsampling rate. Otherwise, we continue by comparing the low-frequency and high-frequency energy of the first $2N$ Fourier modes. This algorithm is continued until the low-frequency energy exceeds the high-frequency energy, or the maximum upsampled rate of 16 is reached. The algorithm is outlined in Algorithm 2.

Algorithm 2 Choose upsampling rate for computing traction jump

Require: \mathbf{x}
 // Input current configuration \mathbf{x}
 $\mathbf{x} \leftarrow \text{upsample } \mathbf{x}$ Upsample by a pre-specified rate of 16
 $\mathcal{B}\mathbf{x} = \text{fourthDeriv}(\mathbf{x})$ Compute the fourth arc-length derivative of the upsampled shape
 $\widehat{\mathcal{B}\mathbf{x}} = \text{fft}(\mathcal{B}\mathbf{x})$ Compute the FFT of the arc-length derivative
 $\alpha = 1.5$ Upsample by at least 1.5
 $\text{low_energy} = \|\widehat{\mathcal{B}\mathbf{x}}(1 : \alpha N/2)\|$ Energy in low frequencies
 $\text{high_energy} = \|\widehat{\mathcal{B}\mathbf{x}}(\alpha N/2 + 1 : \alpha N)\|$ Energy in high frequencies
while ($\text{high_energy} > \text{low_energy} \ \& \ \alpha \leq 16$) **do**
 $\alpha = \alpha + 0.5$ Increase the upsampling rate
 $\text{low_energy} = \|\widehat{\mathcal{B}\mathbf{x}}(1 : \alpha N/2)\|$ Energy in low frequencies
 $\text{high_energy} = \|\widehat{\mathcal{B}\mathbf{x}}(\alpha N/2 + 1 : \alpha N)\|$ Energy in high frequencies
end while
return α

While the upsampling rate may be as large as 16, the vesicle shape is only tracked at the low resolutions with N points. Therefore, the additional cost of computing the traction jump with our anti-aliasing algorithm is proportional to the upsampling rate. In addition, our numerical examples never required an upsampling rate larger than 10, and, at most time steps, they do not exceed 3.

In Figure 2 we use Algorithm 2 to compute the aliasing error in the traction jump of a single elliptical vesicle. To compute the error, we first compute a reference traction jump with 1024 points. Then, we compute the traction jump, but with $N = 12, 16, 24$, and, 32 points both with (red) and without (blue) anti-aliasing. As expected, smaller values of N require a larger upsampling rate. In addition, the error of the Fourier modes of the traction jump when our upsampling algorithm is applied is bounded in the interval $[10^{-6}, 10^{-4}]$ for all four values of N ; in contrast, when no upsampling is applied, the error decays in the low frequencies as N is increased, but remains large in the high frequencies. Finally, even when a high resolution such as $N = 32$ is used, we see that it is important to upsample by at least 1.5 to control the aliasing error.

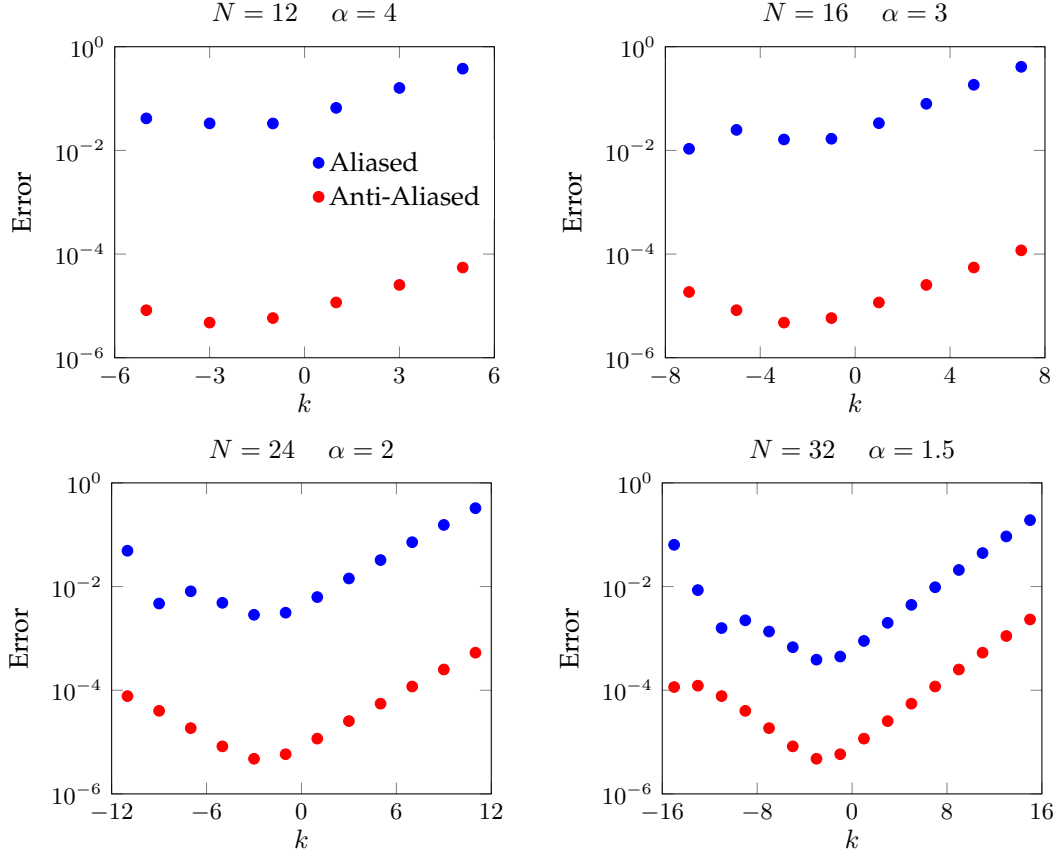


Figure 2: Aliasing error of the traction jump both with and without upsampling at different resolutions. With our anti-aliasing algorithm, the aliasing error is controlled and mesh-independent. Because of symmetry in the geometry, all the even indexed Fourier modes vanish.

For the layer potentials, applying Algorithm 2 is too expensive. Even if we used a low resolution such as $N = 12$, this would require a dense matrix-vector multiplication with 192 points. Therefore, we simply fix an upsampling rate that is used at all resolutions. We have experimented with upsampling by a factor of 2 and upsampling by a factor of $\lceil \sqrt{N} \rceil$. We use the latter value since we have found that the additional cost is offset by the number of rejected time steps in some of our numerical examples. In Figure 3, we plot aliasing errors with and without upsampling, again for an ellipse, and the density function is the vesicle shape. By upsampling to $N^{3/2}$, the error is controlled at all frequencies for all the resolutions. Moreover, the upsampling rate used is less than 6 for the four small values of N that we will be considering.

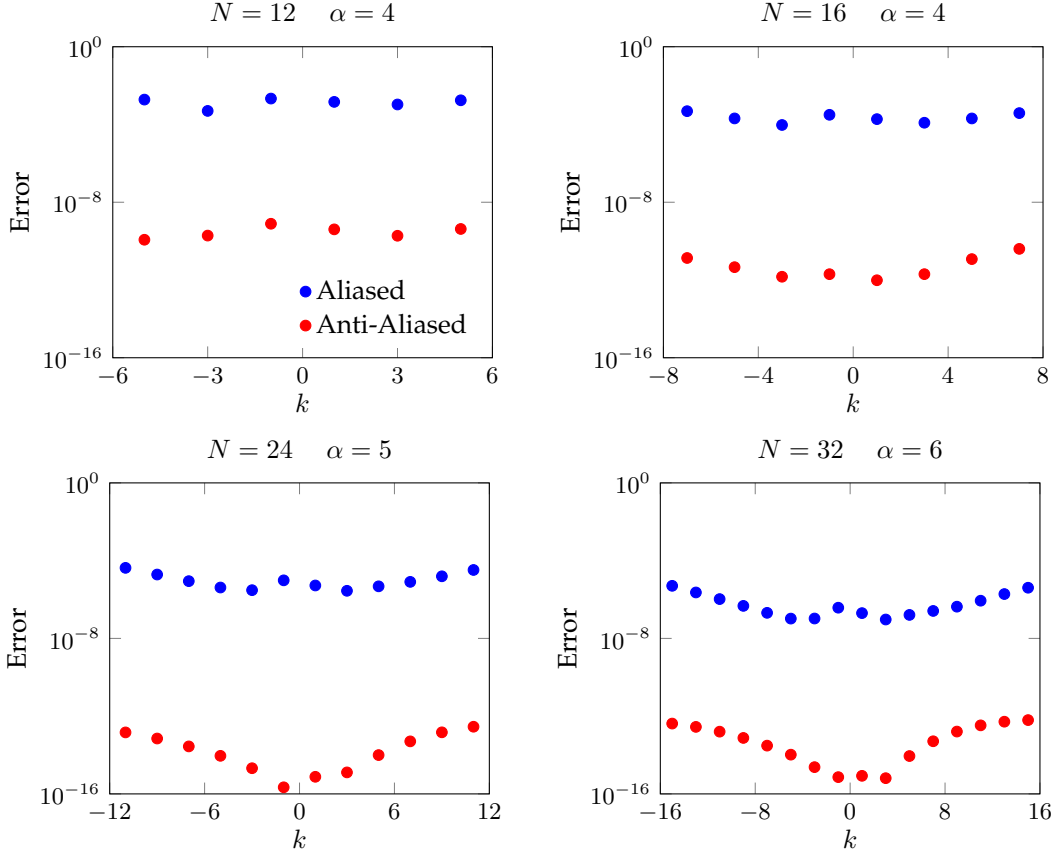


Figure 3: Aliasing error of the single layer potential both with and without upsampling at different resolutions. With our anti-aliasing algorithm, the aliasing error is controlled. Because of symmetry in the geometry, all the even indexed Fourier modes vanish.

3.2. Adaptive time stepping

In [43, 44], we presented an adaptive high-order time stepping method for vesicle suspensions. The scheme uses the errors in the vesicles' area and length to estimate the local truncation error. This is possible since the area and length are invariant by the incompressibility and inextensibility conditions, respectively. The major advantage is that this estimate can be computed with spectral accuracy, basically for free, and, in contrast to many adaptive time stepping methods [18], only one numerical solution is formed. High order accuracy can be achieved through spectral deferred correction (SDC) sweeps [44].

This algorithm poses two issues that need to be addressed in the context of the present study. One issue is that the original proposed algorithm [44] uses asymptotic estimates of the error, so it assumes that the temporal error dominates the spatial error, and that Δt is sufficiently small. The time stepping error does not always dominate in low-resolution simulations, and even if it does, it is possible that a very small Δt is necessary to be in the asymptotic regime. Therefore, before adjusting the time step size, we check if we are in the asymptotic regime. If we are, we use the method proposed in [44], and if not, then we simply increase or decrease the time step size by a constant factor. Moreover, we do not expect to achieve second- or higher-order accuracy in time, and this must be accounted for when adjusting the time step size. The second issue is that the algorithm assumes accumulation of errors in area and length. However, to maintain stability, we will be correcting these errors at every time step. This is easily resolved by specifying a error tolerance for each time step rather than for the time horizon as done in [44].

In Algorithm 3, we describe our new scheme that uses errors in area and length to accept or reject a solution and selects a new time step size. Let ρ_{AL} be the user-defined tolerance for errors in each vesicle's area and length. The area A and length L of a vesicle at time t whose boundary is $\mathbf{x}(\theta, t) = (x(\theta, t), y(\theta, t))$ is

$$A = \frac{1}{2} \int_0^{2\pi} (xy_\theta - yx_\theta) d\theta, \quad L = \int_0^{2\pi} \sqrt{x_\theta^2 + y_\theta^2} d\theta.$$

Shortly we will require dA/dt and dL/dt to adjust the time step. The time derivatives are given by

$$\frac{dA}{dt} = \frac{1}{2} \int_0^{2\pi} (uy_\theta + xv_\theta - vx_\theta - yu_\theta) d\theta, \quad \frac{dL}{dt} = \int_0^{2\pi} \frac{x_\theta u_\theta + y_\theta v_\theta}{\sqrt{x_\theta^2 + y_\theta^2}} d\theta,$$

where $u = \frac{dx}{dt}$ and $v = \frac{dy}{dt}$. We approximate the velocities with

$$u(t) = \frac{x(t + \Delta t) - x(t)}{\Delta t}, \quad v(t) = \frac{y(t + \Delta t) - y(t)}{\Delta t}.$$

Suppose we compute the solution at time $t + \Delta t$ with the first-order time stepping scheme and the solution $\mathbf{x}(t + \Delta t)$ has area $A(t + \Delta t)$ and length $L(t + \Delta t)$. The errors in area and length are

$$\epsilon_A = \frac{|A(t + \Delta t) - A(t)|}{A(t)}, \quad \epsilon_L = \frac{|L(t + \Delta t) - L(t)|}{L(t)}. \quad (5)$$

Assuming $\epsilon_A > \epsilon_L$ (the same argument holds if the situation is reversed), we either accept or reject the solution and choose a new time step size for a single vesicle (we take the maximum errors over all vesicles if we have multiple vesicles) as follows:

1. We, first, check for any collisions between different vesicles and between vesicles and solid walls using the technique presented in [42]. If there is a collision, we reject the solution and decrease the time step size by a factor of two.
2. We define an interval $[\rho_{\min}, \rho_{AL}]$ where $\rho_{\min} = 0.5\rho_{AL}$. We accept the solution if $\rho_{\min} \leq \epsilon_A \leq \rho_{AL}$, and the time step size is not changed. This step helps reduce the number of rejected time steps since it does not increase the time step size when the error is close to the tolerance ρ_{AL} .
3. If $\epsilon_A < \rho_{\min}$, we check if the time step size is in the asymptotic regime. This is done by examining the Taylor series of the area

$$A(t + \Delta t) = A(t) + \frac{dA}{dt}(t) \Delta t + \mathcal{O}(\Delta t^2). \quad (6)$$

We check if the right-hand side in (6) is dominated by the first two terms by defining $q_A(t) = |\frac{dA}{dt}(t) / A(t)|$ so that

$$\epsilon_A \leq q_A(t) \Delta t + |\mathcal{O}(\Delta t^2)|.$$

Then, we say that Δt is in the asymptotic regime if

$$\frac{|\epsilon_A - q_A \Delta t|}{\epsilon_A} \leq \rho_{\text{up}}, \quad (7)$$

and the new time step size is

$$\Delta t_{\text{new}} = \frac{\rho_{AL}}{q_A(t)}. \quad (8)$$

If condition (7) is not satisfied, then we increase the time step size by a constant factor β_{up} . Finally, we do not allow the time step size to exceed the maximal value Δt_{max} .

4. If $\epsilon_A > \rho_{AL}$, we reject the solution and decrease the time step size. Again, we first check if the time step size is in the asymptotic regime. If

$$\frac{|\epsilon_A - q_A \Delta t|}{\epsilon_A} \leq \rho_{\text{down}},$$

then the new time step size is chosen as in (8). Otherwise, we decrease the time step size by a constant factor β_{down} .

At low resolutions, collisions are likely as the hydrodynamic forces may not have been resolved sufficiently. In addition to the collision detection [42] in this scheme, we introduce a repulsion force in Section 3.6 to handle the collisions.

As a final step, we do not allow equation (8) to set a time step size below some minimal value, denoted by Δt_{min} . While this will result in errors greater than the tolerance, the area and length of the vesicles will be corrected at every time step (Section 3.3). If an imminent collision requires a smaller time step size, then the spatial resolution is not sufficient and hence we terminate the simulation.

In summary, we need several parameters in our scheme. First, we need a tolerance ρ_{AL} to decide whether the solution is acceptable. If it is acceptable, then we need to decide if we should increase the time step size. We do this by comparing the error with a tolerance ρ_{min} . If we are to increase the time step size, then we need the tolerance ρ_{up} in (7) to determine if we can use the asymptotic assumption to adjust the time step size using (8). If the asymptotic assumption is not valid, then we need a constant factor β_{up} by which we increase the time step size. If the solution is not acceptable, then we need to decrease the time step size. Similarly, we decide if the asymptotic assumption is valid using a tolerance ρ_{down} . If it is not valid, then we need a constant factor β_{down} by which we decrease the time step size. We list the parameters

Table 1: List of parameters of the adaptive time stepping.

Symbol	Definition	Value
ρ_{AL}	User-defined tolerance for errors in area-length	
ρ_{min}	Tolerance that must be reached for time step to be increased	$\rho_{AL}/2$
β_{up}	Maximum factor of increment in time step size	1.2
β_{down}	Minimum factor of decrement in time step size	0.5
ρ_{up}	Tolerance for using the asymptotic assumption to increase time step size	10^{-3}
ρ_{down}	Tolerance for using the asymptotic assumption to decrease time step size	10^{-2}
Δt_{max}	Maximum time step size	2
Δt_{min}	Minimum time step size	10^{-4}

of the adaptive time stepping and their values in Table 1. Here, we want to be aggressive in decreasing the time step size but cautious in increasing it. Therefore, we choose $\rho_{\text{up}} < \rho_{\text{down}}$. The other parameters are chosen by running a few experiments and choosing values that minimize the total number of rejected time steps. The parameter values in Table 1 work very well for a variety of problems we have tested. We apply the proposed adaptive time stepping scheme to a confined and unconfined suspension in Figure 4.

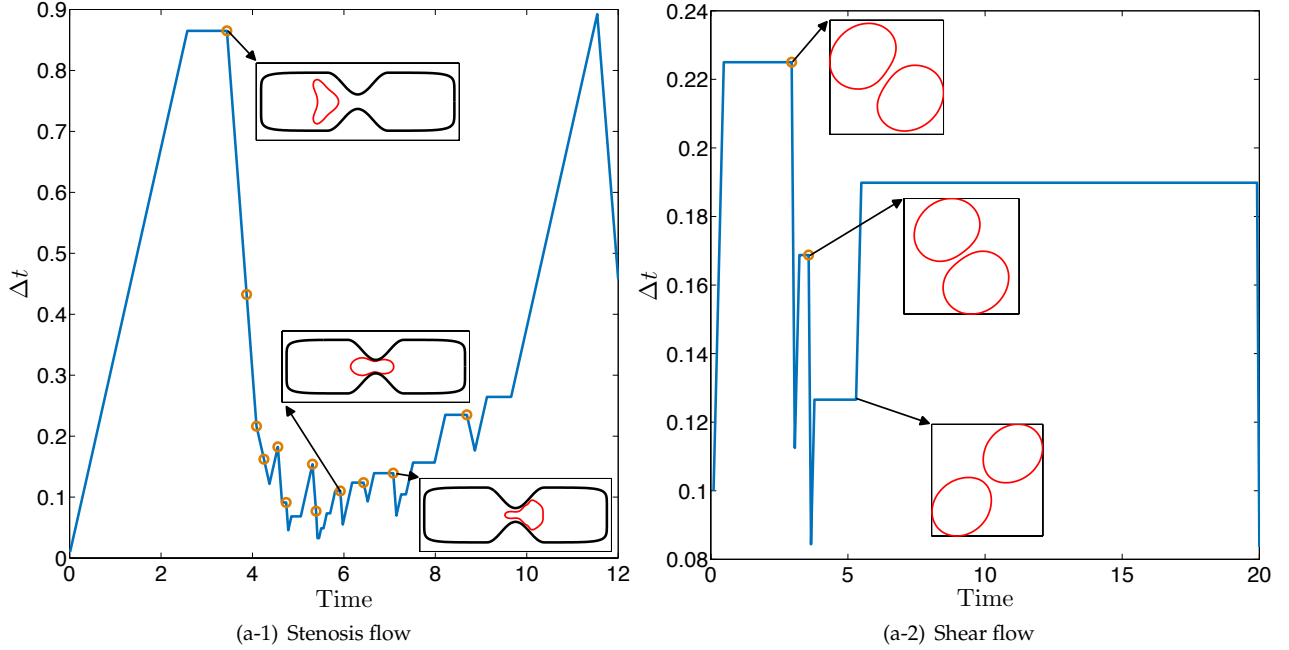


Figure 4: We demonstrate how the time step size varies in a **stenosis flow** (left) and a **shear flow** (right). Open circles indicate the times when a time step size is rejected. In both simulations, vesicles are discretized with $N = 16$ points, and the tolerance is $\rho_{AL} = 10^{-2}$. In the stenosis flow, the outer wall is discretized with $N_{\text{wall}} = 256$ points. There are 12 rejected and 64 accepted time steps in the stenosis flow, and 2 rejected and 110 accepted time steps in the shear flow.

3.3. Local corrections to area and length

The incompressibility and inextensibility conditions guarantee that the area and length of each vesicle are constant. However, long time horizon simulations suffer from the accumulation of errors in area and length which often leads to instabilities or non-physical simulations. Therefore, area-length correction is essential in long time horizon simulations at low resolutions. One way is to add a correction term to the inextensibility condition to correct the length and solve a quadratic equation to correct the area [30]. Another way is to add a forcing term to the inextensibility condition [1, 6, 8]. Here, we introduce a postprocessing technique that maintains the errors in area and length below a prescribed tolerance without modifying the governing equations. This is done with a constrained optimization problem where the constraints require the vesicle's area and length to be fixed.

Suppose that a vesicle initially has area A_0 and length L_0 , and that $\mathbf{x}(t)$ is the solution at time t . We make a local correction to the vesicle's shape by applying sequential quadratic programming (SQP) to

$$\underset{\substack{\tilde{\mathbf{x}}(t) \\ A(\tilde{\mathbf{x}}(t))=A_0 \\ L(\tilde{\mathbf{x}}(t))=L_0}}{\operatorname{argmin}} \|\tilde{\mathbf{x}}(t) - \mathbf{x}(t)\|^2, \quad (9)$$

to obtain a new shape $\tilde{\mathbf{x}}$. Equation (9) is solved iteratively with a MATLAB built-in function, `fmincon`, which is used for minimum constrained algebraic equations (see Algorithm 4 and Algorithm 5). The function requires tolerances for the objective function ρ_{fun} and for the constraints ρ_{con} . In our low-resolution simulations, both tolerances are 10^{-3} . After correcting the area and length, it is possible that vesicles are closer than a minimum distance set by our repulsion force (see Section 3.6). Since we will be treating repulsion explicitly, the result would be a stiffer system and a smaller time step size would be required. To avoid

Algorithm 3 newTimeStepSize($\mathbf{x}_{n+1}, \mathbf{x}_n, \Delta t_n$)

Require: $\rho_{AL}, \rho_{min}, \Delta t_{max}, \Delta t_{min}, \beta_{up}, \beta_{down}, \rho_{up}, \rho_{down}$
// Input current and previous configurations $\mathbf{x}_{n+1}, \mathbf{x}_n$ and previous time step size Δt_n
// Suppose there is a single vesicle and find the new time step size based on error in area, first.
crossing = detectCollision(\mathbf{x}_{n+1}) Check for collisions
if crossing **then** If there is a collision
 accept = false Do not accept the solution
 $\Delta t_{new} = 0.5\Delta t_n$ Decrease Δt
 if $\Delta t_{new} < \Delta t_{min}$ **then** If collision requires $\Delta t < \Delta t_{min}$
 break Resolution is not sufficient, so terminate simulation
 end if
else If there is no collision, check error in area
 $[A_{n+1}, A_n] \leftarrow \text{getArea}(\mathbf{x}_{n+1}, \mathbf{x})$ Compute area of \mathbf{x}_{n+1} and \mathbf{x}_n
 $[q_A, q_L] \leftarrow \text{computeTimeDerivatives}(\mathbf{x}_{n+1})$ Compute $q_A = \left| \frac{dA}{dt} \right| / A$ analytically
 $\epsilon_A \leftarrow \text{computeError}(A_{n+1}, A_n)$ Compute error in area (5)
 if $\rho_{min} \leq \epsilon_A \leq \rho_{AL}$ **then** If error falls into the buffer zone
 accept = true
 $\Delta t_{new} = \Delta t_n$ Accept the solution and do not change the time step size
 else if $\epsilon_A < \rho_{min}$ **then** If error is less than the minimum tolerance
 accept = true Accept the solution
 if $\frac{|\epsilon_A - q_A \Delta t|}{\epsilon_A} \leq \rho_{up}$ **then** If asymptotic assumption is valid
 $\Delta t_{new} = \rho_{AL} / q_A$ Increase Δt based on the asymptotic assumption
 else If asymptotic assumption is not valid
 $\Delta t_{new} = \beta_{up} \Delta t_n$ Increase Δt by a constant factor
 end if
 $\Delta t_{new} = \min(\Delta t_{new}, \Delta t_{max})$ Make sure that Δt is not greater than Δt_{max}
 else if $\epsilon_A > \rho_{AL}$ **then** If error is greater than tolerance
 accept = false Do not accept the solution
 if $\frac{|\epsilon_A - q_A \Delta t_n|}{\epsilon_A} \leq \rho_{down}$ **then** If asymptotic assumption is valid
 $\Delta t_{new} = \rho_{AL} / q_A$ Decrease Δt based on the asymptotic assumption
 else If asymptotic assumption is not valid
 $\Delta t_{new} = \beta_{down} \Delta t_n$ Decrease Δt by a constant factor
 end if
 $\Delta t_{new} = \max(\Delta t_{new}, \Delta t_{min})$ Make sure that Δt is not less than Δt_{min}
 end if
end if
// Repeat for ϵ_L to obtain another Δt_{new} and choose the smaller of the two time step sizes.
// If there are multiple vesicles, then we reject the solution if the tolerance is violated by
// at least one vesicle and we choose the minimum of Δt_{new} over the vesicles.

return $\Delta t_{new}, \text{accept}$

this issue, we only correct the vesicles shape if the correction does not result in the distance between any two vesicles decreasing below the repulsion length scale.

We demonstrate the effectiveness of the local correction in Figure 5. We consider a single vesicle of reduced area 0.65 in a shear flow with no viscosity contrast. The vesicle tilts to a certain inclination angle and then undergoes a tank-treading motion. We discretize the vesicle with $N = 12$ points and reparametrize (see Section 3.4) its boundary at every time step. We take a time horizon of $T = 30$ so that the vesicle tank-treads approximately 1.5 times. We run the simulation with various tolerances for errors in area and length ρ_{AL} . We plot the maximum of the errors in area and length without the correction (top row), snap-

shots of the vesicle configurations without (middle row) and with (bottom row) the local correction to the vesicle's shape. Without correction, the error grows to $\mathcal{O}(10^{-1})$ at the time horizon, and it is still growing. However, the simulations remains stable and accurate, even with large tolerances, when the vesicle's shape is corrected.

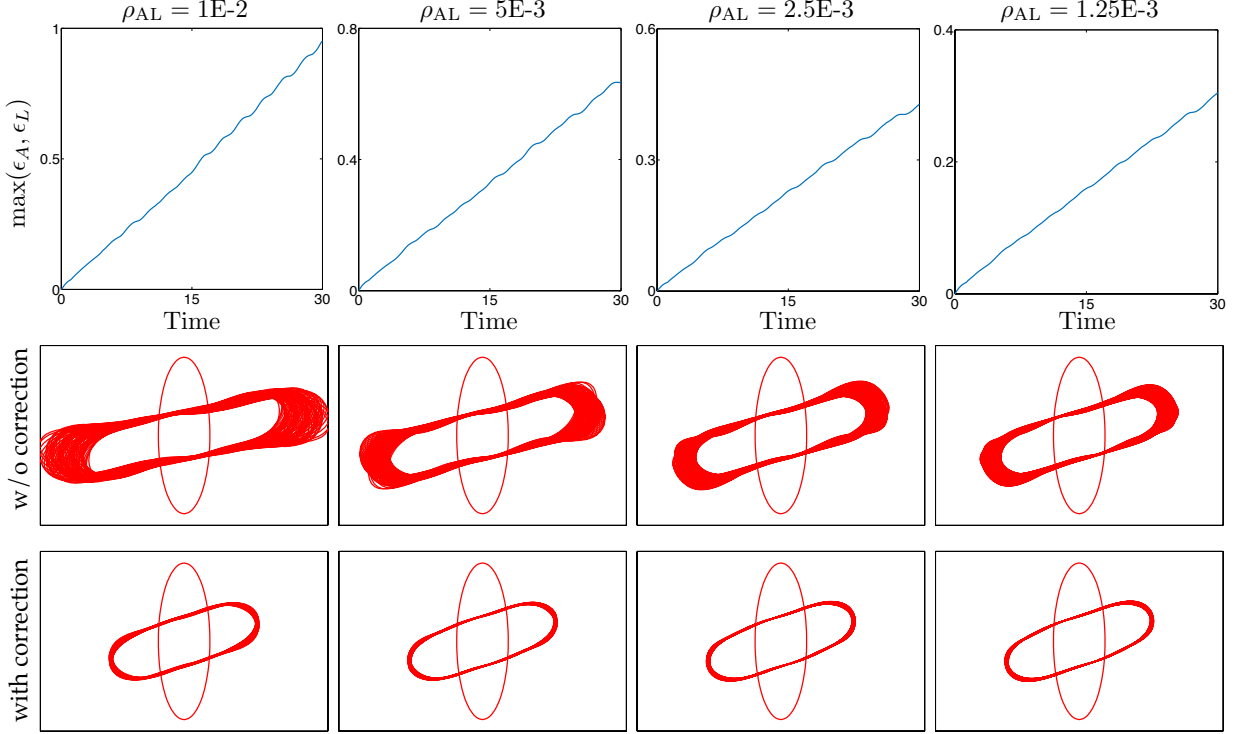


Figure 5: The effect of correcting the vesicle's area and length. We discretize the vesicle with $N = 12$ points. Each column corresponds to a simulation with a tolerance for errors in area and length ρ_{AL} indicated at the top. The top plots are the maximum of the errors in area and length at each time step when the vesicle's shape is not locally corrected and the middle plots show superimposed snapshots. The bottom row are superimposed snapshots of the vesicles when the shape is corrected at every time step.

3.4. Reparametrization

When a vesicle is discretized at low resolutions, time stepping can quickly distort the point distribution. This introduces high frequency components into the boundary parametrization which leads to aliasing errors and numerical instabilities. Therefore, it is essential to redistribute points so that high-frequency components are minimized. The reparametrization algorithm is presented in our previous work [46, 50] for three-dimensional vesicles. In Algorithm 6 we mimic this algorithm for two-dimensional vesicles¹.

Let γ be the boundary of a vesicle that is parameterized as $\mathbf{x}(s)$ where s is arc-length. Let $F : \mathbb{R}^2 \rightarrow \mathbb{R}$ denote an implicit representation of the surface such that $F(\gamma) = 0$ and ∇F does not vanish. We seek a surface parametrization $\mathbf{y}(s)$ which minimizes the quality measure $E(\mathbf{y}) := \sum_{k=1}^N a_k |\hat{\mathbf{y}}_k|^2$:

$$\operatorname{argmin}_{\mathbf{y} \in C^\infty} E(\mathbf{y}(s)), \quad \text{subject to} \quad F(\mathbf{y}(s)) = 0 \quad \text{for all } s,$$

¹Let us emphasize however that in high spatial resolutions such a correction is not necessary.

Algorithm 4 correctShape(\mathbf{x}, A_0, L_0)

```
// Input the initial area and length of each vesicle  $A_0, L_0$ 
// Choose  $\rho_{\text{con}}, \rho_{\text{fun}}$           Choose tolerances for constraints and function we want to minimize
// Set options of fmincon:          MATLAB's fmincon finds minimum of constrained function
// Use Sequential Quadratic Programming (SQP) algorithm with tolerances  $\rho_{\text{con}}, \rho_{\text{fun}}$ 
for  $k = 1, \dots, m$  do          Loop over vesicles
    minFun = @(z) ||z - xk||2          Construct the function we want to minimize
     $\tilde{\mathbf{x}}_k = \text{fmincon}(\text{minFun}, \dots, @(z)\text{constraints}(\mathbf{z}, A_0, L_0), \text{options})$           Make a local correction
    if fmincon fails then
         $\tilde{\mathbf{x}}_k = \mathbf{x}_k$           If the solver fails, do not correct the  $k^{\text{th}}$  vesicle
    end if
end for
crossing = detectCollision( $\tilde{\mathbf{x}}$ )          Check if there is any collision of corrected shapes
if crossing then          If there is a collision
     $\tilde{\mathbf{x}} = \mathbf{x}$           Do not correct any of the shapes
else
    for  $k = 1, \dots, m$  do          Loop over vesicles
        // Check if there are any vesicles in near zone of  $k^{\text{th}}$  vesicle approaching to that
        // This avoids sudden increases in repulsion forces due to unphysical motions led by correction
        approaching = detectNearCollision( $\tilde{\mathbf{x}}_k$ )
        if approaching then
             $\tilde{\mathbf{x}}_k = \mathbf{x}_k$           Do not correct shape of the  $k^{\text{th}}$  vesicle
        end if
    end for
end if
return  $\tilde{\mathbf{x}}$ 
```

Algorithm 5 constraints(\mathbf{z}, A_0, L_0)

```
 $A_z \leftarrow \text{getArea}(\mathbf{z}), L_z \leftarrow \text{getArcLength}(\mathbf{z})$           Compute area and arc-length of current shape  $\mathbf{z}$ 
cEq = [( $A_z - A_0$ )/ $A_0$   ( $L_z - L_0$ )/ $L_0$ ]          Non-linear equalities
return cEq          Return constraints of the optimization problem
```

where a_k are attenuation coefficients. By introducing the Lagrangian $E(\mathbf{y}) + \int_{\gamma} \lambda F(\mathbf{y})$, the optimality condition is obtained by taking the variation of E with respect to \mathbf{y} and λ (see [50]):

$$(I - \mathbf{n}(\mathbf{y}) \otimes \mathbf{n}(\mathbf{y})) \nabla E(\mathbf{y}) = 0 \quad \text{and} \quad F(\mathbf{y}) = 0. \quad (10)$$

We introduce a parameter τ and use pseudo-transient continuation to solve (10). The discretized equation using an explicit scheme is

$$\mathbf{y}_{n+1} = \mathbf{y}_n - \Delta\tau (I - \mathbf{n}(\mathbf{y}_n) \otimes \mathbf{n}(\mathbf{y}_n)) \nabla E(\mathbf{y}_n).$$

Letting $\mathbf{g} = -(I - \mathbf{n}(\mathbf{y}) \otimes \mathbf{n}(\mathbf{y})) \nabla E(\mathbf{y})$, the iteration is continued until the change in \mathbf{y} or the gradient \mathbf{g} is sufficiently small. The parameters $\rho_{\mathbf{y}}$ and $\rho_{\mathbf{g}}$ in Algorithm 6 set this stopping criteria.

Since the goal of reparametrization is to smooth the boundary γ , the attenuation coefficients a_k should be small for low frequencies and grow for high frequencies. We choose $a_k = k^4$ resulting in $\nabla E(\mathbf{y}) = \sum_{k=1}^N k^4 \hat{\mathbf{y}}_k e^{ik\alpha}$. We have also experimented with $a_k = k^2$, but we found that the resulting shapes could still have undesirable high frequencies (see Figure 6).

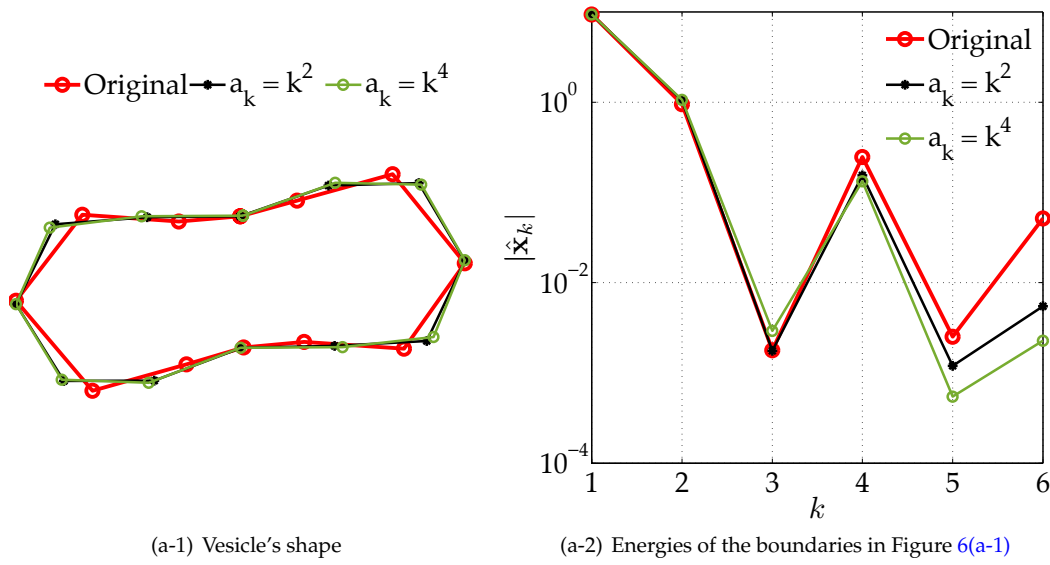


Figure 6: We reports results for two different choices of the attenuation coefficient a_k . We reparametrize the original shape (red) discretized by $N = 12$ points in Figure 6(a-1) with $a_k = k^2$ (black) and $a_k = k^4$ (green). The corresponding shapes are in Figure 6(a-1). Figure 6(a-2) shows the absolute values of the shapes' energies. While the arc-length spacing turns out to be almost uniform with $a_k = k^2$, the additional reduction in the high frequencies from using $a_k = k^4$ results in smoother vesicles and stabler simulations.

In Figure 7, we compare the simulation of two vesicles in a shear flow with and without reparametrization. The vesicles are discretized with $N = 12$ points. We use our new adaptive time stepping scheme (Section 3.2) with a tolerance of $\rho_{AL} = 10^{-2}$ and we correct the area and length of the vesicles after each time step (Section 3.3). The top row does not use reparametrization while the bottom row does. The grey vesicles are from the ground truth. The shapes with reparametrization are significantly smoother and closer to the ground truth. The number of required time steps when we reparametrize is reduced; there are 94 accepted, 4 rejected time steps with reparametrization and 108 accepted, 11 rejected time steps without reparametrization.

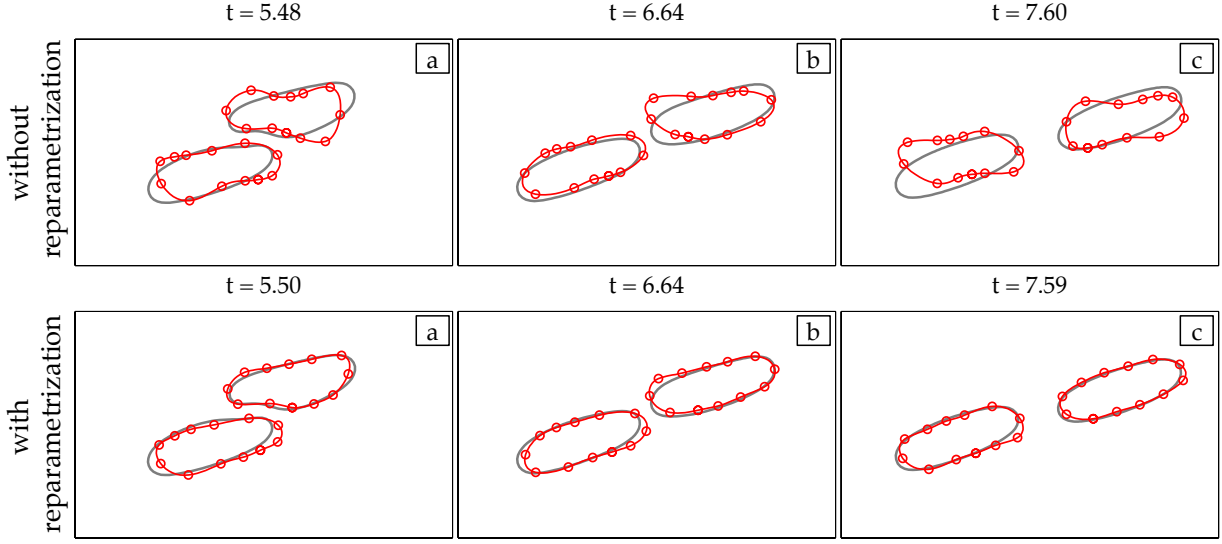


Figure 7: Our reparametrization algorithm applied to two vesicles of reduced area 0.65 in a **shear flow** with no viscosity contrast. Here, the vesicles are discretized with $N = 12$ points and we set $\rho_{AL} = 10^{-2}$. The top row does not use reparametrization while the bottom row does. The grey vesicles are the ground truth solution, which is computed using the high-fidelity version of the code.

Algorithm 6 reparametrize(\mathbf{x})

Require: $\rho_y, \rho_g, \Delta\tau, i_{\max}$
 // We choose $\rho_y = 10^{-3}\Delta\mathbf{x}$ and $\rho_g = 10^{-3}$, where $\Delta\mathbf{x} = \mathbf{u}\Delta t$; and $i_{\max} = 200$
 // We use a line search to find $\Delta\tau$ at every iteration for stability
 $\mathbf{y}_0 \leftarrow \text{upsample } \mathbf{x}$ Upsample to the anti-aliasing frequency
 $\mathbf{g}_0 = -(I - \mathbf{n}(\mathbf{y}_0) \otimes \mathbf{n}(\mathbf{y}_0)) \nabla E(\mathbf{y}_0)$ Projected gradient
 $i = 0$
while $i < i_{\max}$ **do**
 $\mathbf{g} = -(I - \mathbf{n}(\mathbf{y}) \otimes \mathbf{n}(\mathbf{y})) \nabla E(\mathbf{y})$ $\nabla E(\mathbf{y}) = \sum_{k=1}^N k^4 \hat{\mathbf{y}}_k e^{ik\alpha}$
 $\mathbf{y}^+ = \mathbf{y} - \Delta\tau \mathbf{g}$
 $\mathbf{y} \leftarrow \mathbf{y}^+, i \leftarrow i + 1$
 if $\|\mathbf{g}\| < \max(\rho_y/\Delta\tau, \rho_g\|\mathbf{g}_0\|)$ **then**
 break Terminate if the gradient or change in \mathbf{y} is small
 end if
end while
 $\tilde{\mathbf{x}} \leftarrow \text{downsample } \mathbf{y}$ Downsample to the original grid
return $\tilde{\mathbf{x}}$

3.5. Alignment of shapes

Locally correcting (Section 3.3) and reparametrizing (Section 3.4) the vesicle shape often results in translations and rotations. To remove these errors, we apply a rigid body motion to the vesicle shape $\tilde{\mathbf{x}} = (\tilde{x}, \tilde{y})$ after each of the algorithms so that the corrected and reparametrized shape aligns with the original shape. Given a single vesicle, the rigid body motion from $\tilde{\mathbf{x}}$ to \mathbf{x} is

$$\mathbf{x} = R\tilde{\mathbf{x}} + \mathbf{t},$$

where R is a rotation matrix ($R^T R = I$) and \mathbf{t} is a translation vector [7]. To compute R , first let $\mathbf{c}_{\tilde{\mathbf{x}}}$ and $\mathbf{c}_{\mathbf{x}}$ be the centers of the shapes, and then define the 2×2 matrix

$$H = \sum_{i=1}^N (\tilde{\mathbf{x}}_i - \mathbf{c}_{\tilde{\mathbf{x}}}) (\mathbf{x}_i - \mathbf{c}_{\mathbf{x}})^T,$$

where \mathbf{x}_i are the discretization points of the vesicles. By computing the singular value decomposition of $H = U \Sigma V^T$, we obtain the rotation matrix $R = V U^T$. The translation operator \mathbf{t} is, then,

$$\mathbf{t} = -R \mathbf{c}_{\tilde{\mathbf{x}}} + \mathbf{c}_{\mathbf{x}}.$$

The new shape is $\mathbf{x}_{\text{new}} = R \tilde{\mathbf{x}} + \mathbf{t}$ which, in addition to having the correct area, length, and a smooth boundary, has the same center and inclination angle as the shape prior to these local corrections. Therefore, this algorithm helps minimize the artificial effects of the correction algorithms on the dynamics given by the governing equations.

3.6. Repulsion

While hydrodynamic forces do not allow vesicles to cross, these forces are often not accurately resolved in simulations with low spatial resolutions, and vesicles may collide. We introduce a repulsion force to handle collisions. We use discrete penalty layers to penalize close proximity between discretization points on vesicles. The form of the repulsion we use has been introduced for contact mechanics [19, 51]. Letting h_{max} be the maximum arc-length spacing and δ_{min} a repulsion length scale, the repulsion force does not allow vesicles to be closer than $d_{\text{min}} = \delta_{\text{min}} h_{\text{max}}$. We define a gap function for discrete layer ℓ between two discretization points $\mathbf{x} \in \gamma_p$ and $\mathbf{y} \in \gamma_q$, $p \neq q$

$$g_\ell = \|\mathbf{r}\| - \frac{d_{\text{min}}}{\ell},$$

where $\|\mathbf{r}\| = \|\mathbf{x} - \mathbf{y}\|$. The gap function measures the proximity of two points on the vesicles (γ_p and γ_q). When $g_\ell < 0$, the points are in the proximity of the layer ℓ . The repulsion force for being in the proximity of the ℓ^{th} discrete layer is penalized with

$$\mathbf{F}^\ell = \begin{cases} -2W\ell^2 \frac{g_\ell}{\|\mathbf{r}\|} \mathbf{r}, & \text{if } g_\ell < 0, \\ 0, & \text{otherwise,} \end{cases} \quad (11)$$

where W is the repulsion strength.

The penalty force can be considered as placing a spring between approaching vesicles. If there is a single spring between them, the spring will compress fully and eventually fail for sufficiently large relative velocity. However, having penalty forces as a function of the active discrete layers as in (11) can be considered as placing an infinite number of springs between approaching vesicles. This guarantees that two vesicles do not collide, which renders the method robust. Although this guarantee is independent of the repulsion strength W , performance of the method and error in physics depend on the choice of W .

The total number of activated discrete layers, L , is the largest integer less than $\frac{d_{\text{min}}}{\|\mathbf{r}\|}$. Hence, the total penalty force on point $\mathbf{x} \in \gamma_p$ due to point $\mathbf{y} \in \gamma_q$ is

$$\mathbf{F} = \sum_{\ell=1}^L \mathbf{F}^\ell = W \left(-\frac{L(L+1)(2L+1)}{3} + L(L+1) \frac{d_{\text{min}}}{\|\mathbf{r}\|} \right) \mathbf{r}, \quad L = \left\lfloor \frac{d_{\text{min}}}{\|\mathbf{r}\|} \right\rfloor \quad (12)$$

In Figure 8 we plot the total number of discrete layers activated L and the total penalty force of two approaching points. We show each L in Figure 8(a-1) and the corresponding total penalty force \mathbf{F} in Figure 8(a-2) with the same color. As the points approach to each other, the number of activated layers L increases and the color of the curves showing L and \mathbf{F} simultaneously change. Finally, the repulsion force at a point $\mathbf{x} \in \gamma_p$ due to all other vesicles is formed by summing (12) over all discretization points $\mathbf{y} \notin \gamma_p$.

We treat the repulsion force explicitly. That is, single layer potentials of the repulsion forces are computed and placed on the right hand side of the linear system. While this can lead to stiffness, it has never been an issue in our actual experiments.

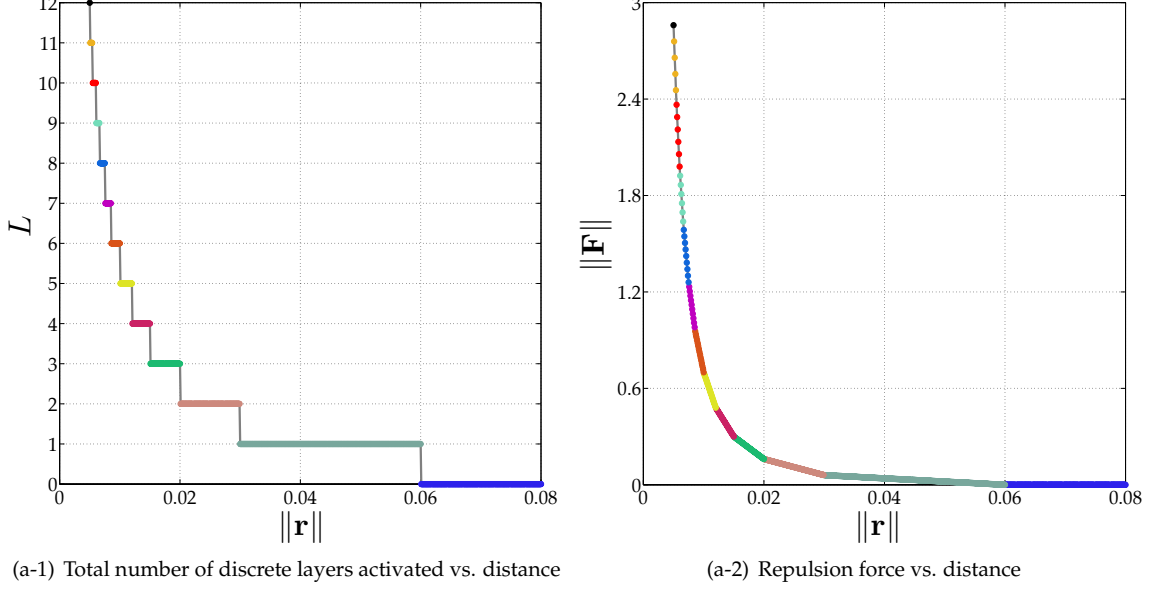


Figure 8: Here we take two approaching points and compute the total number of activated discrete layers L and the total penalty force \mathbf{F} (see (12)). We choose $d_{\min} = 0.06$ and $W = 1$. We show each L on the left and magnitude of the corresponding total penalty force $\|\mathbf{F}\|$ on the right with the same color. The repulsion force increases as the points approach each other.

Remark. In order to choose the repulsion length scale δ_{\min} , we place two vesicles of reduced area 0.65 symmetrically about the origin in an extensional flow. This simulation is done at a low resolution with $N = 12$ points. We examine the energy in the six lowest frequencies relative to the total energy of the hydrodynamic interaction. This ratio is used to heuristically set δ_{\min} . In this example, when the vesicle separation is less than $0.3h_{\max}$, this ratio drops significantly and high-frequency components appear. Therefore, we set the repulsion length scale to $\delta_{\min} = 0.3$ implying that the minimum distance between vesicles is $d_{\min} = 0.3h_{\max}$ after which the repulsion force is non-zero. We set the repulsion strength W so that the velocity of the repulsion force is 10% of the velocity due to all hydrodynamic forces. Other ratios were tried, but larger values did not allow vesicles to come sufficiently close, and smaller values introduced too much stiffness. While vesicles can approach one another in various ways, this example represents one of the worse case scenarios since the proximity between the vesicles decreases for all time, and we have successfully used this length scale parameter for all of our experiments in Section 4.

4. Numerical experiments

In this section, we demonstrate with various examples that the low-resolution correction algorithms (LRCA) introduced in Section 3 are necessary to maintain stability and to increase accuracy at low spatial resolution. We discuss the accuracy of the low-resolution simulations in terms of different error measures. The error measures are discussed in Section 4.1, and a summary of the numerical experiments are in Section 4.2.

4.1. Error measures

In our previous work [42, 44, 45, 50], we use the errors in the area and length of the vesicles to measure the accuracy. However, since we correct the area and length of vesicles at each time step, this error measure becomes obsolete. We present two new sets of error measures, one for dilute suspensions and one for dense suspensions.

For dilute suspensions, we are interested in the accuracy of the vesicle configuration. We examine the convergence of the method to a ground truth, where the ground truth is formed at high resolutions with small error tolerances [44]. We summarize the error measures for dilute suspensions in Table 2, and then discuss details of each measure.

Table 2: List of error measures for dilute suspensions.

Symbol	Definition	Formulation
ϵ_{center}	Error in the center of a vesicle	(13)
ϵ_{prox}	Error in the proximity of two vesicles	(14)
ϵ_{IA}	Error in the inclination angle of a vesicle	(15)

Let $\hat{\mathbf{x}}_k$ and \mathbf{x}_k , $k = 1, \dots, m$, denote the position of m vesicles formed with a high-resolution simulation (ground truth) and with a low-resolution simulation, respectively. If $\hat{\mathbf{c}}_k$ and \mathbf{c}_k are the centers of the vesicles, then the error over all time of the center of vesicle k , and the maximum of this error over all vesicles are

$$\epsilon_{\text{center}}^k = \max_{t \in [0, T]} \begin{cases} \frac{\|\mathbf{c}_k - \hat{\mathbf{c}}_k\|_2}{\varepsilon}, & \text{if } \|\hat{\mathbf{c}}_k\|_2 = 0 \\ \frac{\|\mathbf{c}_k - \hat{\mathbf{c}}_k\|_2}{\|\hat{\mathbf{c}}_k\|_2}, & \text{otherwise} \end{cases}, \quad \epsilon_{\text{center}} = \max_{k=1, \dots, m} \epsilon_{\text{center}}^k, \quad (13)$$

where ε is MATLAB's floating point relative accuracy `eps`.

The error in proximity is used for examples with two vesicles. Letting $\mathbf{d} = \mathbf{c}_1 - \mathbf{c}_2$ and $\hat{\mathbf{d}} = \hat{\mathbf{c}}_1 - \hat{\mathbf{c}}_2$, the error in proximity of the two vesicles is

$$\epsilon_{\text{prox}} = \max_{t \in [0, T]} \frac{\|\mathbf{d} - \hat{\mathbf{d}}\|_2}{\|\hat{\mathbf{d}}\|_2}. \quad (14)$$

The inclination angle (IA) is the angle between the x -axis and the principal axis corresponding to the smallest principal moment of inertia [45]. The moment of inertia tensor is

$$J = \int_{\omega} (|\mathbf{r}|^2 I - \mathbf{r} \otimes \mathbf{r}) d\mathbf{x} = \frac{1}{4} \int_{\gamma} \mathbf{r} \cdot \mathbf{n} (|\mathbf{r}|^2 I - \mathbf{r} \otimes \mathbf{r}) ds,$$

where $\mathbf{r} = \mathbf{x} - \mathbf{c}$, and \mathbf{c} is the center of the vesicle. Then the error over all time of the inclination angle of the k^{th} vesicle, and the maximum over all vesicles are

$$\epsilon_{\text{IA}}^k = \max_{t \in [0, T]} \begin{cases} \frac{|\text{IA}_k - \widehat{\text{IA}}_k|}{\varepsilon}, & \text{if } |\widehat{\text{IA}}_k| = 0 \\ \frac{|\text{IA}_k - \widehat{\text{IA}}_k|}{|\widehat{\text{IA}}_k|}, & \text{otherwise} \end{cases}, \quad \epsilon_{\text{IA}} = \max_{k=1, \dots, m} \epsilon_{\text{IA}}^k. \quad (15)$$

For dense suspensions, the error in the vesicles' configurations at low resolutions is large and irrelevant. However, depending on the purpose of the simulation, low-resolution simulations can provide significant information with a considerably low computational cost. We consider upscaling measures such as errors in statistics and space-time averages of physical quantities. A list of error measures for dense suspensions are in Table 3.

Table 3: List of error measures for dense suspensions.

Symbol	Definition	Formulation
$\epsilon_{\langle v \rangle}$	Error in the space-time average of a velocity field	(16), (17)
$\epsilon_{\langle V \rangle}$	Error in the time average of the L^2 norm of a velocity field	(18), (19)
$\epsilon_{\mu_{\text{eff}}}$	Error in the effective viscosity of a suspension	(20), (21), (22)

The velocity field of the fluid bulk plays an important role in many applications. For instance, in [21] we study mixing in a Couette apparatus containing vesicles (see Figure 18). We model transport with an advection-diffusion equation, so capturing the correct averages of the velocity field is crucial. We consider the error in space-time average of the velocity field and the error in time average of the L^2 norm of the velocity field.

The space and space-time averages of a velocity field $\mathbf{V}(\mathbf{x}, t)$ are

$$v(t) = \frac{1}{|\Omega|} \int_{\Omega} \mathbf{V}(\mathbf{x}, t) d\mathbf{x}, \quad \langle v \rangle = \frac{1}{T} \int_0^T v(t) dt, \quad (16)$$

respectively. Letting $\langle \hat{v} \rangle$ and $\langle v \rangle$ denote the space-time averages of velocity fields given by a ground truth and its corresponding low-resolution simulations, the error is

$$\epsilon_{\langle v \rangle} = \frac{|\langle v \rangle - \langle \hat{v} \rangle|}{|\langle \hat{v} \rangle|}. \quad (17)$$

Additionally, the L^2 norm of the velocity field and the time average of this quantity are

$$V(t) = \frac{1}{|\Omega|} \left(\int_{\Omega} \mathbf{V}^2(\mathbf{x}, t) d\mathbf{x} \right)^{\frac{1}{2}}, \quad \langle V \rangle = \frac{1}{T} \int_0^T V(t) dt, \quad (18)$$

respectively. The error in the time average of the L^2 norm of a velocity field is

$$\epsilon_{\langle V \rangle} = \frac{|\langle V \rangle - \langle \hat{V} \rangle|}{|\langle \hat{V} \rangle|}. \quad (19)$$

Another error measure is based on a numerical homogenization for suspension rheology. The effective viscosity of a suspension is the viscosity of a homogeneous Newtonian fluid having the same energy dissipation per macroscopic volume element. For vesicle suspensions, it is given by [45]

$$\mu_{\text{eff}} = \mu_0 + \phi \frac{1}{T} \int_0^T \bar{\sigma}_{12}^p dt \quad (20)$$

where

$$\bar{\sigma}^p = \frac{1}{|\Omega|} \int_{\gamma} [-(\kappa_b \kappa^2 \mathbf{n} \otimes \mathbf{n} + \sigma \mathbf{t} \otimes \mathbf{t}) + \mu_0(\nu - 1)(\mathbf{u} \otimes \mathbf{n} + \mathbf{n} \otimes \mathbf{u})] ds. \quad (21)$$

Here, μ_0 is viscosity of the bulk fluid, ϕ is the volume fraction of vesicles, $\bar{\sigma}^p$ is the spatial average of the perturbation in stress σ due to the presence of vesicles, κ_b is the bending stiffness, κ is the curvature, \mathbf{n} , \mathbf{t} are the unit normal and tangent vectors, and \mathbf{u} is the velocity. Letting $\hat{\mu}_{\text{eff}}$ and μ_{eff} be effective viscosities of a suspension obtained from a ground truth and a low-resolution simulation, the error in effective viscosity of a suspension is

$$\epsilon_{\mu_{\text{eff}}} = \frac{|\mu_{\text{eff}} - \hat{\mu}_{\text{eff}}|}{|\hat{\mu}_{\text{eff}}|}. \quad (22)$$

For dense suspensions in a Couette apparatus, we also report probability distribution functions of the location of each vesicle's center and the magnitude of the velocity at certain radii.

4.2. Summary of numerical experiments

We perform numerical experiments of both dilute and dense vesicle suspensions in bounded and unbounded domains. We use our adaptive time stepping in all runs except when forming the ground truth. Then, we compare the simulations with and without the LRCA introduced in Section 3. We report timings and the errors defined in Tables 2 and 3. A simulation is stopped if our adaptive time stepping algorithm requires a time step size less than $\Delta t = 10^{-8}$. The examples we consider are:

- **Two vesicles in a shear flow** (Section 4.3): We simulate a pair of vesicles with viscosity contrasts $\nu = 1$ and $\nu = 10$ and reduced areas (RA) 0.65 and 0.99. The initial configurations result in the vesicles nearly touching. The purpose of these experiments is to demonstrate errors in average quantities such as the proximity between vesicles and the actual trajectories of the vesicles.
- **One vesicle in a stenosis flow** (Section 4.4): We simulate a single vesicle of reduced area 0.65 and without viscosity contrast $\nu = 1$ in a constricted tube (stenosis) with a parabolic flow profile at the intake and the outtake.
- **Four vesicles in a Taylor-Green flow** (Section 4.5): We simulate four vesicles of reduced area 0.65 with viscosity contrasts of $\nu = 1$ and $\nu = 10$ in a periodic Taylor-Green flow. The vesicles cover approximately 50% of the area of a periodic cell $(0, \pi)^2$ making vesicle interactions stronger and the problem more complicated than the previous examples.
- **Couette apparatus** (Section 4.6): We simulate vesicles of reduced area 0.65 without viscosity contrast in a Couette apparatus. Simulations with volume fractions $\phi = 20\%$ and $\phi = 40\%$ are performed. For these examples, we report errors in the upscaled quantities (see Table 3) and statistics.

For complex flows, the LRCA are essential to maintain stability, achieve sufficient accuracy and maintain physical vesicle shapes at low resolutions. As resolution increases, the effects of the LRCA on the dynamics disappear and the simulations with the LRCA converge to the ground truth. We note, however, that the definition of low resolution is problem dependent. That is, it is not obvious at what resolution the LRCA are not needed for a given problem beforehand. For example, in our shear examples, $N \geq 16$ is sufficient to have stable simulations and hence we do not need the LRCA. However, for the stenosis flow, the use of the LRCA provides better accuracy and shorter CPU time even at $N = 32$.

Remark. For all runs, we fix the bending stiffness to $\kappa_b = 10^{-1}$ and the GMRES tolerance to $\rho_{\text{GMRES}} = 10^{-10}$. Ground truth solutions computed with the high-fidelity version of the code are illustrated as grey vesicles. Additionally, since we use our adaptive time stepping scheme, simulations are compared at different, but comparable times.

4.3. Shear flow

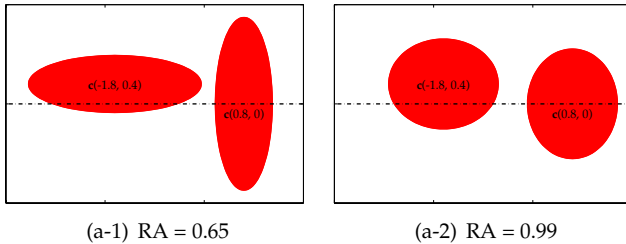


Figure 9: The initial configurations of two vesicles in an unbounded shear flow $\mathbf{u} = (y, 0)$. The left plot has vesicles of reduced area 0.65 and the right plot has vesicles of reduced area 0.99. Both these simulations are run with viscosity contrasts $\nu = 1$ and $\nu = 10$.

Parameter	Value
Points on a vesicle N	96
Viscosity contrast ν	$\{1, 10\}$
Number of SDC sweeps $n_{\text{sd}}c$	1
Time step size Δt	5×10^{-4}
CPU time (RA = 0.65, $\nu = 1$)	17 hours
CPU time (RA = 0.65, $\nu = 10$)	61 hours
CPU time (RA = 0.99, $\nu = 1$)	16 hours
CPU time (RA = 0.99, $\nu = 10$)	36 hours

Table 4: Parameters of the ground truth of a shear flow.

Setup. We consider two vesicles in an unbounded shear flow $\mathbf{u} = (y, 0)$. The initial configuration (Figure 9) results in the left vesicle traveling to the right and over top of the right vesicle. We consider reduced areas 0.65 and 0.99 and viscosity contrasts $\nu = 1$ and $\nu = 10$. We simulate each of these cases with $N = 12, 16, 24, 32$ points per vesicle and an error tolerance $\rho_{\text{AL}} = 10^{-2}, 10^{-3}, 10^{-4}, 10^{-5}$ with and without the algorithms in Section 3. The time horizon is $T = 20$ so that the vesicles pass one another. The ground truth solutions are formed with the parameters in Table 4.

Results. We investigate the necessity of the LRCA to maintain stability and we quantify their effect on the error in the proximity of the vesicles, ϵ_{prox} . This problem is particularly difficult because the hydrodynamic force is inaccurate at low resolutions, and this can cause vesicles to collide. We report the errors in proximity, the number of accepted and rejected time steps, and the CPU times.

In Table 5, we summarize the simulations of two vesicles of reduce area 0.65 with $\nu = 1$ (top) and $\nu = 10$ (bottom). For almost all the simulations, the LRCA are not necessary to maintain stability. However, the error in the proximity of the vesicles is decreased when the LRCA are used for all runs except $N = 32$ with $\nu = 1$, and for the two highest resolutions with $\nu = 10$. In these cases where the simulations with the LRCA have greater errors in the proximity than the original simulations, the resolution is sufficient for stability without the LRCA and the effects of the LRCA do not vanish. That's why, the original simulations are more accurate than the ones with the LRCA. In addition, as expected, the CPU time is increased when the algorithms are used, but the payoff is additional stability and accuracy in almost all the examples. Figure 10 shows snapshots of the simulation without viscosity contrast at one resolution both with and without our algorithms, and it is clear that the LRCA are necessary to maintain physical vesicle shapes. In Figure 11 the two vesicles with $\nu = 10$ are illustrated at three different resolutions with the LRCA. Here we see convergence towards the ground truth when the resolutions are increased.

Table 5: The errors in the proximity of two vesicles of RA = 0.65 with viscosity contrast $\nu = 1$ (top) and $\nu = 10$ (bottom) in a **shear flow** with and without the LRCA in Section 3 (see Figures 10 and 11). Also reported are the number of accepted and rejected time steps and the CPU time. The simulation with $\nu = 10$ and $N = 16$ breaks without the LRCA because collisions cannot be handled.

$\nu = 1$									
N	ρ_{AL}	LRCA				Original			
		ϵ_{prox}	Accepts	Rejects	Time (sec)	ϵ_{prox}	Accepts	Rejects	Time (sec)
12	1E-2	1.2E-1	94	4	64	2.5E-1	128	10	58
16	1E-3	3.7E-2	310	7	193	2.0E-1	345	14	132
24	1E-4	4.1E-2	998	11	826	4.1E-2	1026	14	400
32	1E-5	2.8E-2	3156	15	1930	9.1E-3	3174	15	808

$\nu = 10$									
N	ρ_{AL}	LRCA				Original			
		ϵ_{prox}	Accepts	Rejects	Time (sec)	ϵ_{prox}	Accepts	Rejects	Time (sec)
12	1E-2	3.9E+0	93	9	60	3.0E+0	98	11	41.4
16	1E-3	1.1E+0	227	19	205	-	-	-	-
24	1E-4	3.1E-1	786	32	843	1.6E-1	773	31	438
32	1E-5	1.4E-1	2567	37	2660	3.7E-2	2480	35	1120

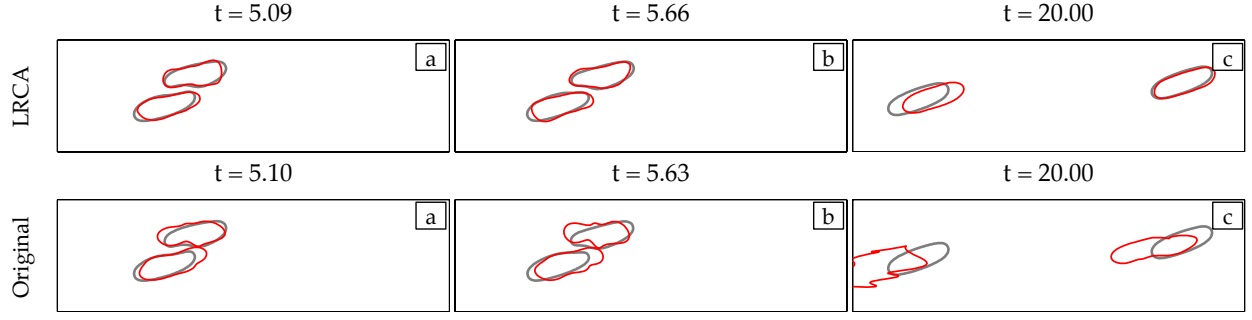


Figure 10: Two vesicles with reduced area 0.65, viscosity contrast $\nu = 1$, and discretized with $N = 12$ points in a **shear flow**. The error tolerance is $\rho_{AL} = 10^{-2}$ and the grey vesicles are the ground truth. In the top row, the LRCA are used, and in the bottom row, they are not. The error metric we are using seems to be underestimating the error. Although the error in proximity can be considered reasonable, the original simulation has non-physical vesicles.

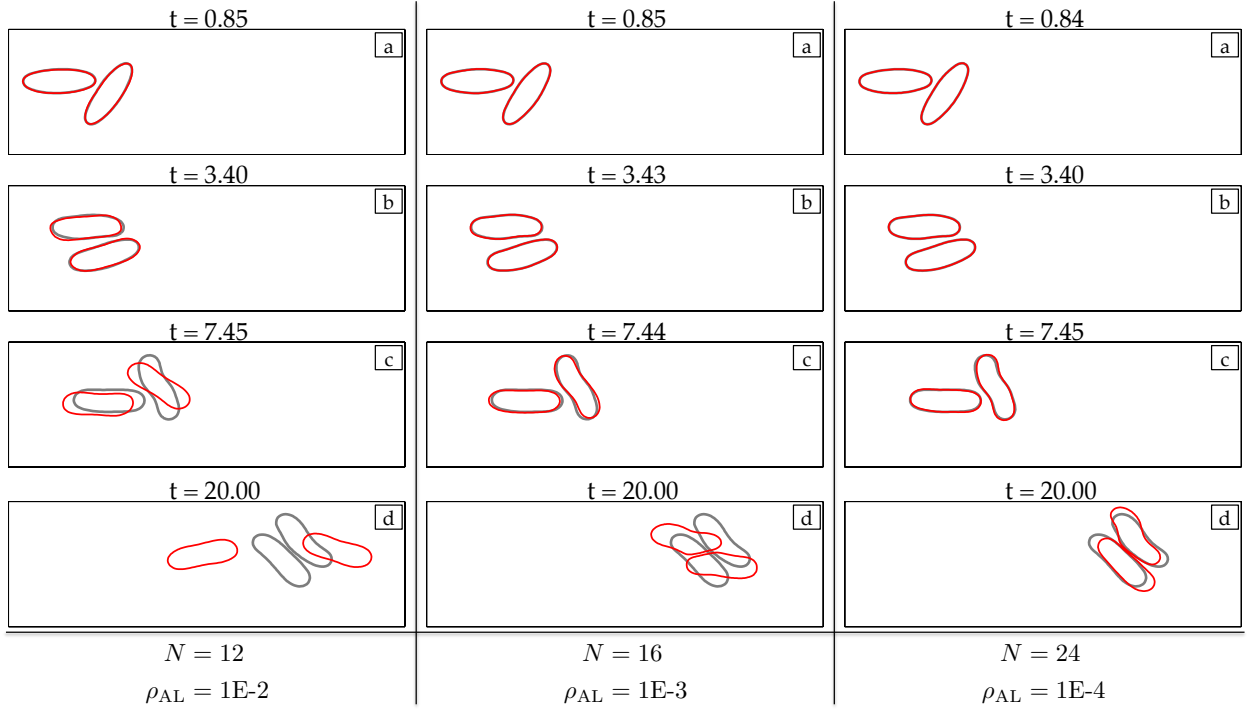


Figure 11: Two vesicles with RA = 0.65 and $\nu = 10$ in a **shear flow** using the LRCA. Vesicles are discretized with $N = 12, 16, 24$ points and the error tolerances in area and length are $\rho_{AL} = 10^{-2}, 10^{-3}, 10^{-4}$, respectively. The grey vesicles are from the ground truth. Here, we show that as the resolution increases, the artificial effects of the LRCA on the dynamics vanish and the simulations with the LRCA converge to the ground truth.

Finally, we present results for the vesicles of reduced area 0.99 with the two different viscosity contrasts in Table 6. Here, vesicles do not come as close as those of reduced area 0.65. At all the resolutions we consider, not using the LRCA delivers more accurate results in terms of the vesicles' proximity with less CPU time. However if the algorithms are not used at the resolutions $N \leq 16$, the errors in area and length of the vesicles are $\mathcal{O}(10^{-1})$. This leads the vesicles to have non-physical shapes at the time horizon (see

Figure 12 and Figure 13).

Table 6: The error in the proximity of two vesicles of $RA = 0.99$ with viscosity contrast $\nu = 1$ (top) and $\nu = 10$ (bottom) in a **shear flow** with and without the LRCA in Section 3 (see Figure 12 and Figure 13 for frames of the simulations at the coarsest resolution). Also reported are the number of accepted and rejected time steps and the CPU time.

		$\nu = 1$							
		LRCA				Original			
N	ρ_{AL}	ϵ_{prox}	Accepts	Rejects	Time (sec)	ϵ_{prox}	Accepts	Rejects	Time (sec)
12	1E-2	5.3E-1	110	2	57	5.5E-1	110	3	38
16	1E-3	3.4E-1	373	3	199	1.1E-1	343	6	134
24	1E-4	6.5E-2	1192	9	699	1.5E-2	1191	9	446
32	1E-5	1.8E-2	3766	13	2300	4.8E-3	3767	13	862

		$\nu = 10$							
		LRCA				Original			
N	ρ_{AL}	ϵ_{prox}	Accepts	Rejects	Time (sec)	ϵ_{prox}	Accepts	Rejects	Time (sec)
12	1E-2	6.8E-1	99	3	52	3.8E-1	93	4	38
16	1E-3	3.0E-1	318	7	181	7.5E-2	318	7	127
24	1E-4	1.2E-1	1030	7	668	9.4E-3	1030	7	384
32	1E-5	1.1E-2	3160	8	2250	3.2E-3	3160	8	972

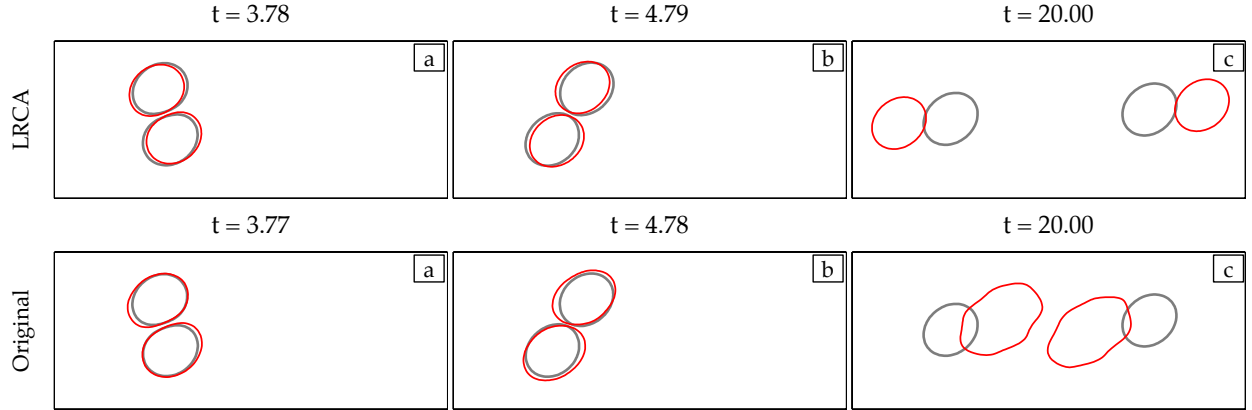


Figure 12: Two vesicles with reduced area 0.99, viscosity contrast $\nu = 1$, and discretized with $N = 12$ points in a **shear flow**. The error tolerance is $\rho_{AL} = 10^{-2}$ and the grey vesicles are the ground truth. In the top row, the LRCA are used, and in the bottom row, they are not. Similar to simulations shown in Figure 10, although the errors in the proximity are very close with and without the LRCA at these resolutions ($N = 12$ and $\rho_{AL} = 1E - 2$), the LRCA are necessary to maintain physical vesicle shapes.

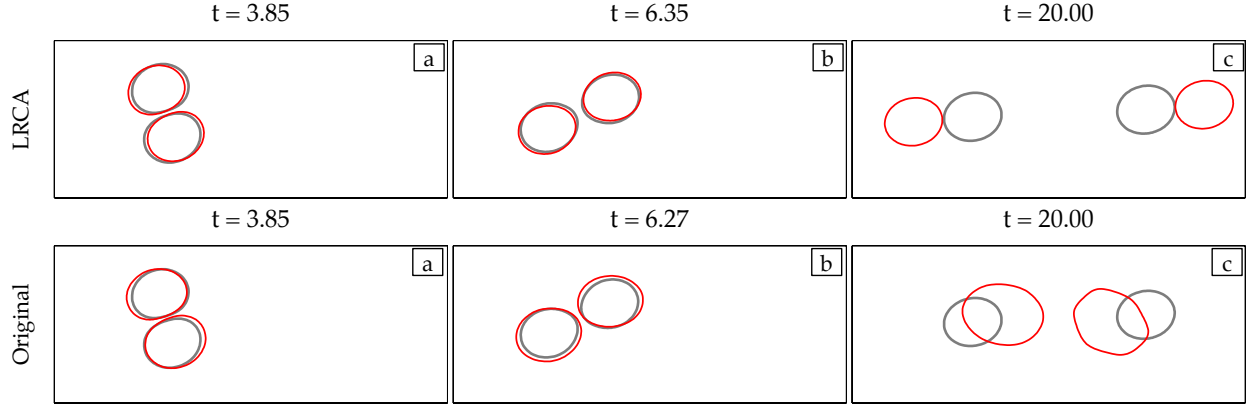


Figure 13: Two vesicles with reduced area 0.99, viscosity contrast $\nu = 10$, and discretized with $N = 12$ points in a **shear flow**. The error tolerance is $\rho_{\Delta L} = 10^{-2}$ and the grey vesicles are the ground truth. In the top row, the LRCA are used, and in the bottom row, they are not.

4.4. Stenosis flow

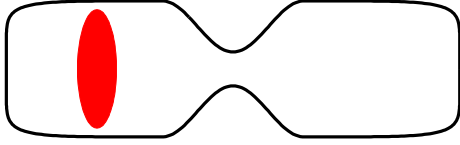


Figure 14: The initial configuration of a **stenosis flow**.

Parameter	Value
Points on a vesicle N	128
Points on a wall N_{wall}	480
Number of SDC sweeps $n_{\text{sd}}c$	1
Time step size Δt	10^{-3}
CPU time	22 hours

Table 7: Parameters of the ground truth of a **stenosis flow**.

Setup. We consider a single vesicle of reduced area 0.65 passing through a constricted tube (stenosis) without viscosity contrast (Figure 14). The flow is driven by a parabolic flow profile at the intake and the outtake and the vesicle's initial height is 3.5 times larger than the size of the constriction. We choose a time horizon $T = 12$ so that the vesicle passes through the constriction. We simulate this example with $N = 12, 16, 24, 32$ points on the vesicle and $N_{\text{wall}} = 256$ points on the wall with and without the LRCA. The ground truth solution is formed with the parameters in Table 7.

Results. We again investigate the stability of our scheme with and without the LRCA. In this example, reparametrization is necessary since the vesicle becomes highly deformed, which results in high frequencies in the shape that need to be removed. Time adaptivity and repulsion are necessary for the vesicle to pass through the constriction without crossing the outer boundary. In Figure 15 plots of the vesicle passing through the constriction at different resolution with the LRCA is qualitatively compared with the ground truth (grey vesicle). Even at the lowest resolution, the vesicle passes through the constriction, and the vesicle shape and center agree quite well with the ground truth. Whereas vesicle-wall collisions cannot be handled without the LRCA and the simulations break at these resolutions (i.e. $N \leq 24$).

We report the errors in the center, the number of accepted and rejected time steps, and the CPU time, both with and without the LRCA in Table 8. We see that without the algorithms, the low-resolution simulations are not stable with $N \leq 24$. At these resolutions, even with a very small time step, the dynamics when the shape is close to the solid wall can not be resolved. However, with the help of the LRCA, the simulations are stable and deliver acceptably accurate results in short CPU times. Even with $N = 32$ where the algorithms are unnecessary for stability, using them reduces the total number of time steps resulting in a computationally faster method.

Table 8: The error in the center of the vesicle in a **stenosis flow** with and without the LRCA in Section 3 (see Figure 15 for frames of these simulations using the algorithms). Also reported are the number of accepted and rejected time steps and the CPU time. The original simulations break when $N \leq 24$ because the vesicle-wall collisions cannot be handled.

N	ρ_{AL}	LRCA				Original			
		ϵ_{center}	Accepts	Rejects	Time (sec)	ϵ_{center}	Accepts	Rejects	Time (sec)
12	1E-1	1.7E-1	29	6	83	-	-	-	-
16	1E-2	8.1E-2	64	12	116	-	-	-	-
24	1E-3	2.6E-2	208	32	348	-	-	-	-
32	1E-4	1.2E-2	567	27	887	1.4E-2	1312	155	1950

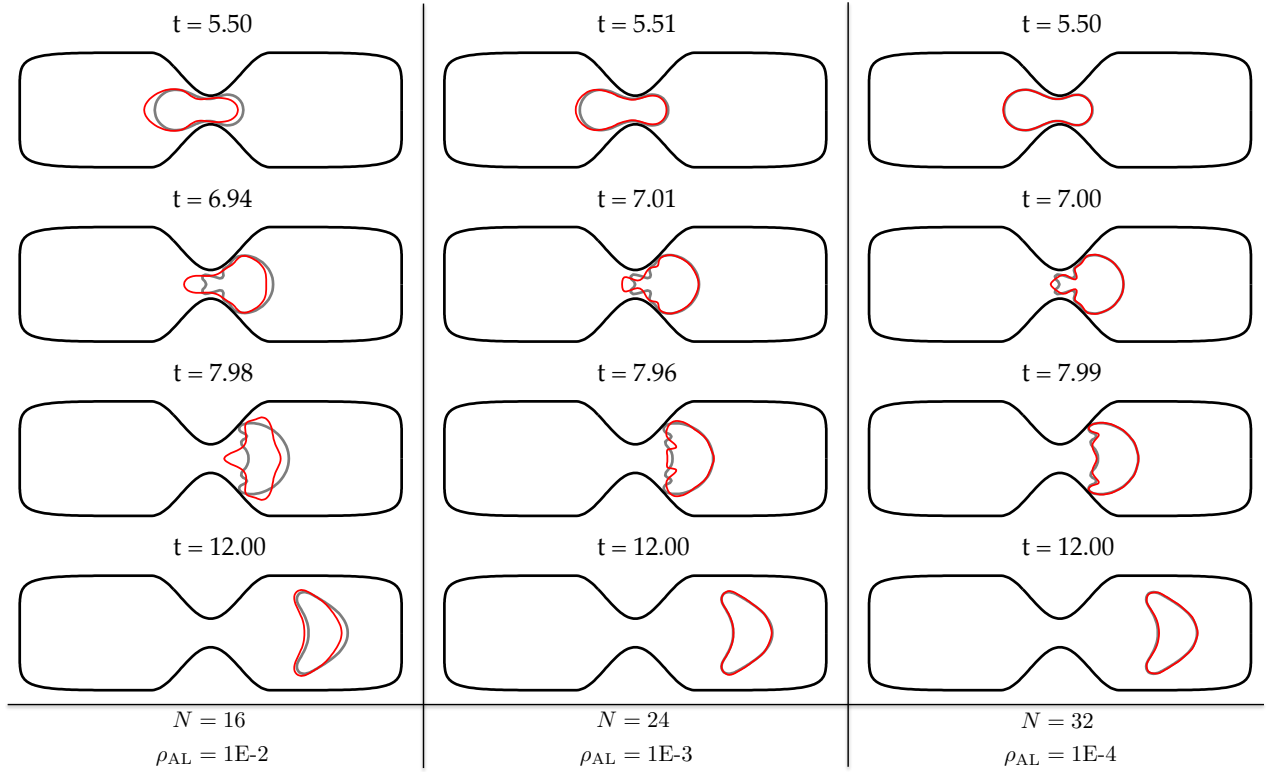


Figure 15: A single vesicle passing through a constricted tube (**stenosis**). Here we vary the temporal and spatial resolutions simultaneously and use the LRCA. The spatial resolution and error tolerances are indicated at the bottom of each column. The wall is discretized with $N_{\text{wall}} = 256$ in all of the simulations. The grey vesicle is the ground truth. While these low-resolution simulations are stable and accurate with the LRCA, vesicle-wall collisions cannot be handled in the original simulations.

4.5. Taylor-Green flow

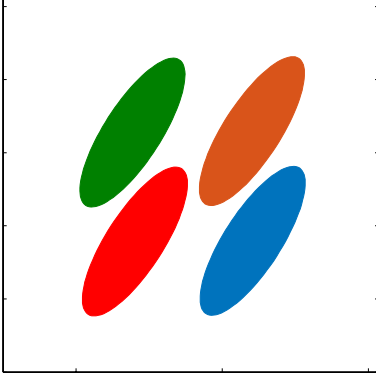


Figure 16: Initial configuration of a **Taylor-Green flow**.

Parameter	Value
Points per vesicle N	64
Viscosity contrast ν	$\{1, 10\}$
Number of SDC sweeps $n_{\text{sd}}c$	1
Time step size Δt	10^{-3}
CPU ($\nu = 1$)	17.2 hours
CPU ($\nu = 10$)	76.4 hours

Table 9: Parameters of the ground truth of a **Taylor-Green flow**.

Setup. We consider four large vesicles of reduced area 0.65 in the periodic cell $(0, \pi)^2$ with the background Taylor-Green flow $\mathbf{u} = (\sin x \cos y, -\cos x \sin y)$. The vesicles occupy about 55% of the periodic cell (see Figure 16). We color each vesicle for tracking purposes. The time horizon is $T = 20$ and we perform simulations with viscosity contrasts $\nu = 1$ and $\nu = 10$. We simulate these examples with $N = 12, 16, 24, 32, 48$ points per vesicle, the error tolerances $\rho_{\text{AL}} = 10^{-1}, 10^{-2}, 10^{-3}, 10^{-4}, 10^{-5}$, with and without the LRCA in Section 3. A ground truth solution for these examples is formed with the parameters in Table 9.

Results. This example is more complex than the previous examples since there are interactions between multiple vesicles. Therefore, we expect that our algorithms are more crucial than the previous examples at low resolutions. We summarize the results of the vesicles with $\nu = 1$ in Table 10 (with the LRCA) and Table 11 (without the LRCA). We report the errors in the vesicles' centers, inclination angles, and effective viscosity, as well as the number of accepted and rejected time steps, and the total CPU time. Also, in Figure 17 we plot snapshots of the vesicle shapes at four different resolutions and superimpose the ground truth solution. We see that the LRCA result in stability at much lower resolutions, but the errors in the center and inclination angle of the vesicles are large (i.e. $\mathcal{O}(1)$). The reason for that is this example has more vesicle-vesicle interactions than the previous two and the near collisions lead to more chaotic flows [3, 33]. Figure 17 shows that the centers and inclination angles of vesicles in the low-resolution simulations are close to those of the ground truth over a short time. As the vesicles interact more, the errors accumulate and result in diverging long-term behavior of an individual vesicle. However, the error of the effective viscosity, which is an upscaled variable, is satisfactory. In contrast, without the LRCA, stability is not achieved until $N = 32$ due to vesicle-vesicle collisions which cannot be handled. Smaller errors can be achieved without the LRCA, but this requires a resolution of $N = 48$.

We repeat these experiments with viscosity contrast $\nu = 10$ and we report the results in Tables 12 and 13. Again, we see that with the LRCA, the errors in the center and inclination angle are large and the error in the viscosity contrast is small. Without the LRCA, stability requires $N = 32$ points, and smaller errors than those with our algorithms requires $N = 48$ points.

Table 10: The maximum errors in the vesicles' centers, inclination angles, and the effective viscosity of four vesicles in a **Taylor-Green flow** with no viscosity contrast (Figure 17) and with the LRCA. Also reported are the number of accepted and rejected time steps and the CPU times.

N	ρ_{AL}	ϵ_{center}	ϵ_{IA}	$\epsilon_{\mu_{\text{eff}}}$	Accepts	Rejects	Time (sec)
12	1E-1	1.0E+0	9.7E-1	4.1E-1	35	7	50
16	1E-2	1.8E+0	2.0E+0	2.9E-2	92	8	106
24	1E-3	1.7E+0	2.1E+0	1.9E-2	326	13	419
32	1E-4	1.6E+0	2.0E+0	1.6E-2	1080	15	1390
48	1E-5	1.5E+0	4.2E-1	1.5E-2	3437	26	5990

Table 11: *The maximum errors in the vesicles' centers, inclination angles, and the effective viscosity of four vesicles in a **Taylor-Green flow** with no viscosity contrast and without the LRCA. Also reported are the number of accepted and rejected time steps and the CPU times. The simulations without the LRCA break for $N \leq 24$ since collisions cannot be handled. The results for the LRCA are in Table 10.*

N	ρ_{AL}	ϵ_{center}	ϵ_{IA}	$\epsilon_{\mu_{\text{eff}}}$	Accepts	Rejects	Time (sec)
12	1E-1	-	-	-	-	-	-
16	1E-2	-	-	-	-	-	-
24	1E-3	-	-	-	-	-	-
32	1E-4	1.5E+0	1.9E+0	1.3E-1	1064	16	736
48	1E-5	5.4E-1	2.8E-1	4.8E-3	3306	29	3480

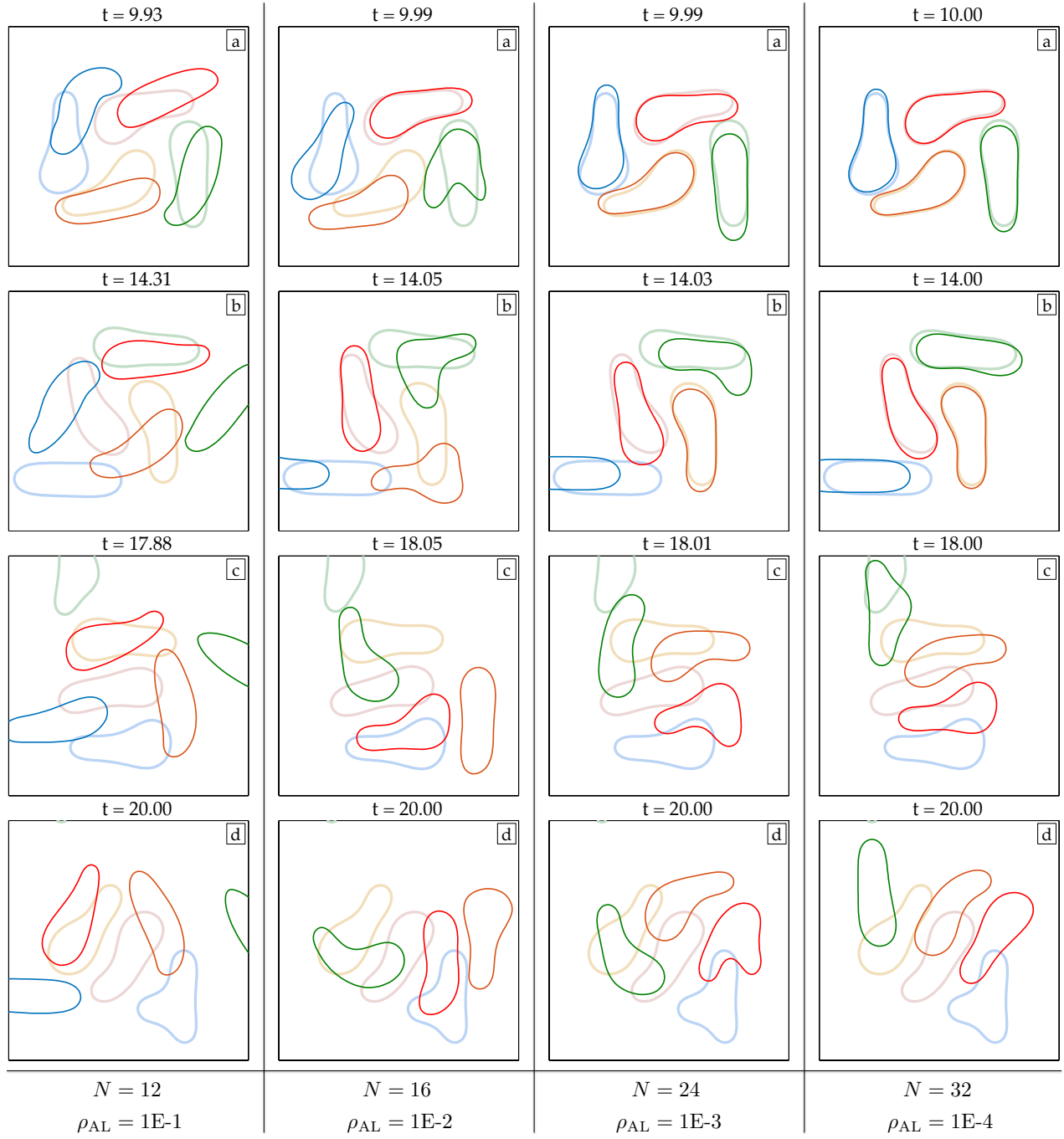


Figure 17: Four vesicles in a **Taylor-Green flow** with no viscosity contrast and with the LRCA. The spatial resolutions and the error tolerances are given at the bottom of each column. Faded vesicles correspond to the ground truth and the low-resolution counterparts are in bright colors.

Table 12: The maximum errors in the vesicles' centers, inclination angles, and the effective viscosity of four vesicles in a **Taylor-Green flow** with viscosity contrast 10 and with the LRCA. Also reported are the number of accepted and rejected time steps and the CPU times.

N	ρ_{AL}	ϵ_{center}	ϵ_{IA}	$\epsilon_{\mu_{eff}}$	Accepts	Rejects	Time (sec)
12	1E-1	2.9E+0	2.0E+0	2.3E-1	36	9	50
16	1E-2	1.6E+0	2.0E+0	8.0E-2	91	7	87
24	1E-3	1.6E+0	5.9E-1	4.8E-2	282	10	371
32	1E-4	3.4E-1	1.2E-1	2.4E-2	881	10	1210
48	1E-5	1.1E-1	5.4E-2	2.1E-2	2835	15	8650

Table 13: The maximum errors in the vesicles' centers, inclination angles, and the effective viscosity of four vesicles in a **Taylor-Green flow** with viscosity contrast 10 and without the LRCA. Also reported are the number of accepted and rejected time steps and the CPU times. The simulations without the LRCA break for $N \leq 24$ since collisions cannot be handled. The results for the LRCA are in Table 12.

N	ρ_{AL}	ϵ_{center}	ϵ_{IA}	$\epsilon_{\mu_{eff}}$	Accepts	Rejects	Time (sec)
12	1E-1	-	-	-	-	-	-
16	1E-2	-	-	-	-	-	-
24	1E-3	-	-	-	-	-	-
32	1E-4	3.8E-1	1.7E-1	1.7E-2	894	11	940
48	1E-5	9.7E-2	5.8E-2	1.4E-2	2786	12	6380

4.6. Couette flow

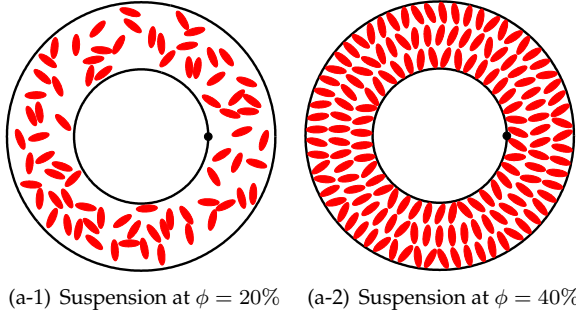


Figure 18: The initial configuration of two **Couette** apparatuses with volume fractions $\phi = 20\%$ and $\phi = 40\%$. For the ground truth solutions, we use the local area-length correction algorithm, but none of the other algorithms introduced in Section 3.

Parameter	Value
Points on a vesicle N	96
Points on a wall N_{wall}	256
Number of SDC sweeps n_{sdc}	1
Time step size Δt	10^{-2}
CPU time($\phi = 20\%$)	3 weeks
CPU time($\phi = 40\%$)	1 month

Table 14: Parameters of the ground truth of a **Couette flow**.

Setup. We consider two Couette flows with volume fractions $\phi = 20\%$ (75 vesicles) and $\phi = 40\%$ (150 vesicles) without viscosity contrast (see Figure 18). The inner boundary has radii $R_1 = 10$ and is rotating with constant angular velocity while the outer boundary has radii $R_2 = 20$ and is stationary. We choose a time horizon $T = 100$ which results in the inner cylinder completing approximately 16 rotations. We simulate these cases with $N = 16, 24$ points per vesicle, $N_{wall} = 128$ points per wall, error tolerances $\rho_{AL} = 10^{-2}, 10^{-3}$, and the LRCA. The ground truth solution for these examples use the parameters in the caption of Figure 18.

Results. A Couette apparatus is often used to investigate properties of suspensions such as shear-induced diffusion [39] and effective viscosity. High volume fraction suspensions are of particular importance since

red blood cells make up approximately 45% of human blood [17]. In addition, long time horizons are required for these flows to reach statistical equilibriums [21]. Therefore, there are a large number of interactions between vesicles and walls, near collisions, and highly deformed vesicles. The interactions and shapes can be resolved with fine resolutions, but at a significant computational cost.

We are interested in the errors of upscaled variables. We report the errors in effective viscosity, space-time average and time average of the L^2 norm of a velocity field in Table 15 for $\phi = 20\%$ and in Table 16 for $\phi = 40\%$. We also present the frames from the simulations of the suspension at $\phi = 20\%$ in Figure 19 and the suspension at $\phi = 40\%$ in Figure 20 at various resolutions. As in the previous example, the actual vesicle centers are not captured by the simulations with the LRCA. However, the errors in the upscaled quantities are at an acceptable level of $\mathcal{O}(10^{-2})$ even with $N = 16$ points on each vesicle. In addition, the computation speedup is significant; the low-resolution runs required no more than a little over a day ($\phi = 20\%$) and less than a week ($\phi = 40\%$). In contrast, the ground truth simulations required 3 weeks ($\phi = 20\%$) and a month ($\phi = 40\%$).

Table 15: The errors in the effective viscosity $\epsilon_{\mu_{\text{eff}}}$, time-space average of the velocity $\epsilon_{\langle v \rangle}$, and the time average of the L^2 norm of the velocity $\epsilon_{\langle V \rangle}$ of a suspension at $\phi = 20\%$ in a **Couette flow** with the LRCA (Figure 19). Also reported are the number of accepted and rejected time steps and the CPU time.

N	ρ_{AL}	$\epsilon_{\mu_{\text{eff}}}$	$\epsilon_{\langle v \rangle}$	$\epsilon_{\langle V \rangle}$	Accepts	Rejects	Time (hours)
16	2E-2	4.2E-2	8.6E-2	2.9E-2	507	74	9.3
16	1E-3	2.5E-2	3.8E-2	1.8E-2	2499	82	32.8
24	2E-2	2.9E-2	7.8E-2	2.3E-2	402	31	10.1
24	1E-3	2.1E-2	3.4E-2	1.7E-2	2160	55	32.2

Table 16: The errors in the effective viscosity $\epsilon_{\mu_{\text{eff}}}$, time-space average of the velocity $\epsilon_{\langle v \rangle}$, and the time average of the L^2 norm of the velocity $\epsilon_{\langle V \rangle}$ of a suspension at $\phi = 40\%$ in a **Couette flow** with the LRCA (Figure 20). Also reported are the number of accepted and rejected time steps and the CPU time.

N	ρ_{AL}	$\epsilon_{\mu_{\text{eff}}}$	$\epsilon_{\langle v \rangle}$	$\epsilon_{\langle V \rangle}$	Accepts	Rejects	Time (hours)
16	1E-2	2.7E-2	1.5E-1	7.2E-2	1007	125	62.8
16	1E-3	1.6E-2	7.8E-2	4.7E-2	3517	110	156.1
24	1E-2	1.9E-2	1.3E-1	5.9E-2	806	37	42.2
24	1E-3	3.1E-3	6.1E-2	3.1E-2	2894	67	138.6

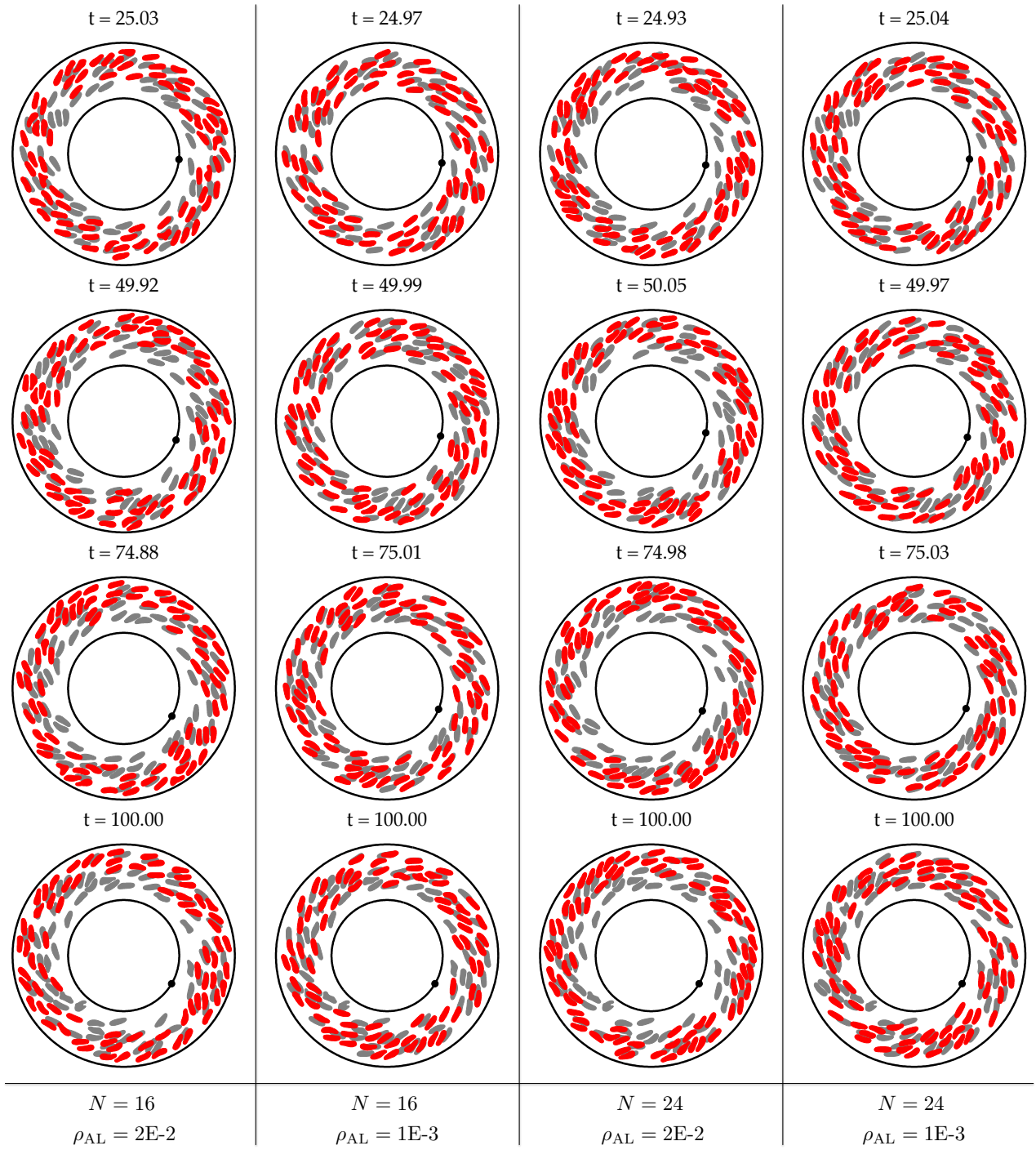


Figure 19: 75 vesicles in a **Couette flow** which corresponds to a volume fraction of $\phi = 20\%$. The ground truth is shown with grey vesicles superimposed with the low-resolution counterpart (red vesicles).

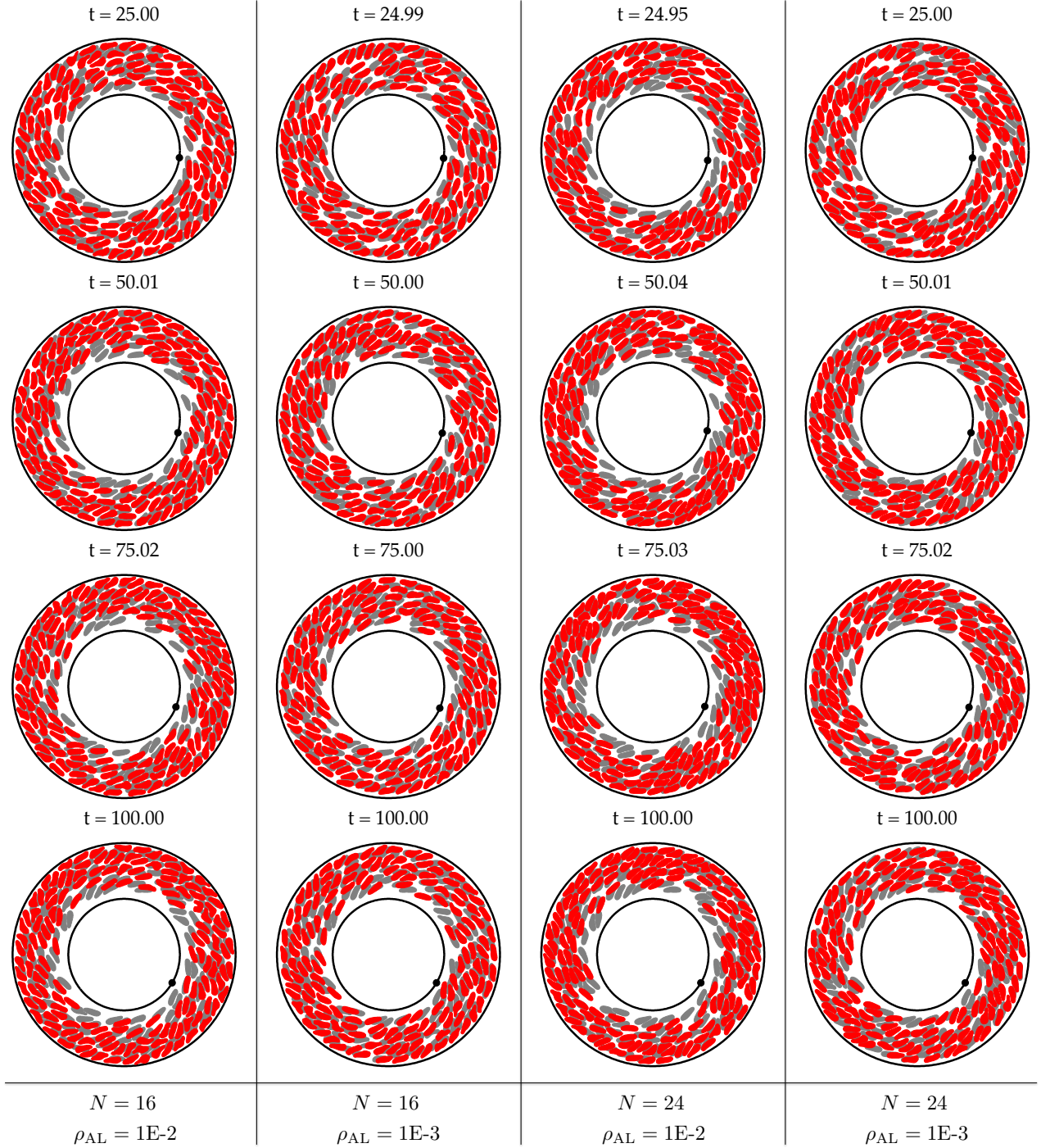


Figure 20: 150 vesicles in a **Couette flow** which corresponds to a volume fraction of $\phi = 40\%$. The ground truth is shown with grey vesicles superimposed with the low-resolution counterpart (red vesicles).

Cell-Free Layer. Next, we investigate how accurately the low-resolution simulations can capture the statistics of the vesicle locations. In this setup, vesicles are known to migrate away from the walls resulting in a so-called cell-free layer near the walls [28]. This layer is captured by our low-resolution simulations at low error tolerances ρ_{AL} (see Figures 19 and 20), but at the high error tolerances the cell-free layer is thicker

than the ground truth (first and third columns). To further demonstrate this point, we plot the probability distribution functions of distances of the vesicles' centers to the origin throughout the simulations in Figure 21. The figure shows that the simulations with the error tolerance $\rho_{AL} = 10^{-3}$ estimate the cell-free layer accurately at both spatial resolutions, while with tolerance $\rho_{AL} = 10^{-2}$, the cell-free layer is larger than the ground truth. This suggests that in order to capture the statistics of dense suspensions, low spatial resolutions are sufficient with high enough temporal resolutions.

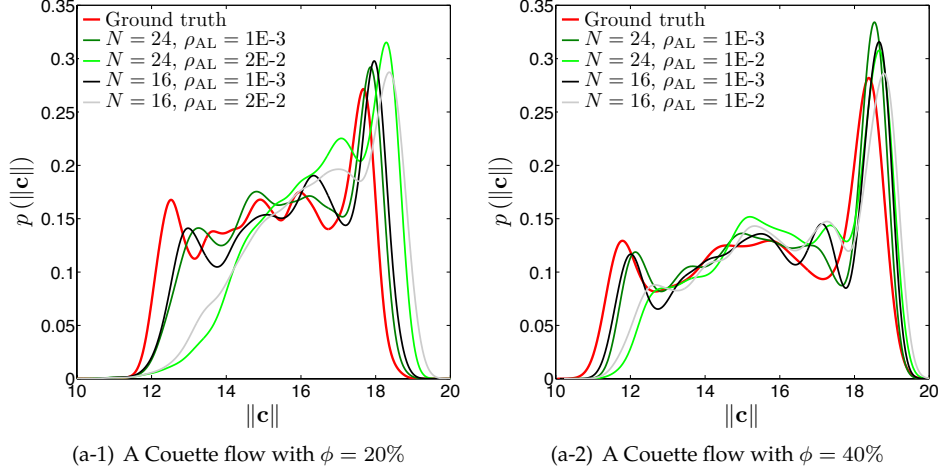


Figure 21: *Statistics of the vesicles' concentration in a Couette flow.* We plot the probability distributions of distances of the vesicles' centers to the origin for the suspensions with volume fractions $\phi = 20\%$ (left) and $\phi = 40\%$ (right).

Statistics of the velocity field. We also use simulations of vesicle suspensions in a Couette apparatus to infer mixing properties of the suspensions [21]. For this reason, it is important to estimate the velocity field accurately. We compute the error in the space-time averages of the velocity field discussed above. In Figure 22 we present statistics of the magnitude of the velocity field, $\|\mathbf{V}\|$, at points equally distributed in the azimuthal direction at three different radii ($\frac{r-R_1}{R_2-R_1} = 0.2, 0.5, 0.8$). Then we plot the probability distribution function of $\|\mathbf{V}\|$ in Figure 22. In the absence of vesicles, \mathbf{V} is only a function of the radial position in a Couette flow. However, the presence of vesicles perturbs the velocity field. The low-resolution simulations with the error tolerances $\rho_{AL} = 10^{-3}$ estimate the statistics of the velocity field closely. Similar to the statistics to capture the cell-free layer (Figure 21), higher temporal resolutions provide more accurate velocity statistics while the spatial resolution does not significantly affect the results (see Figure 22).

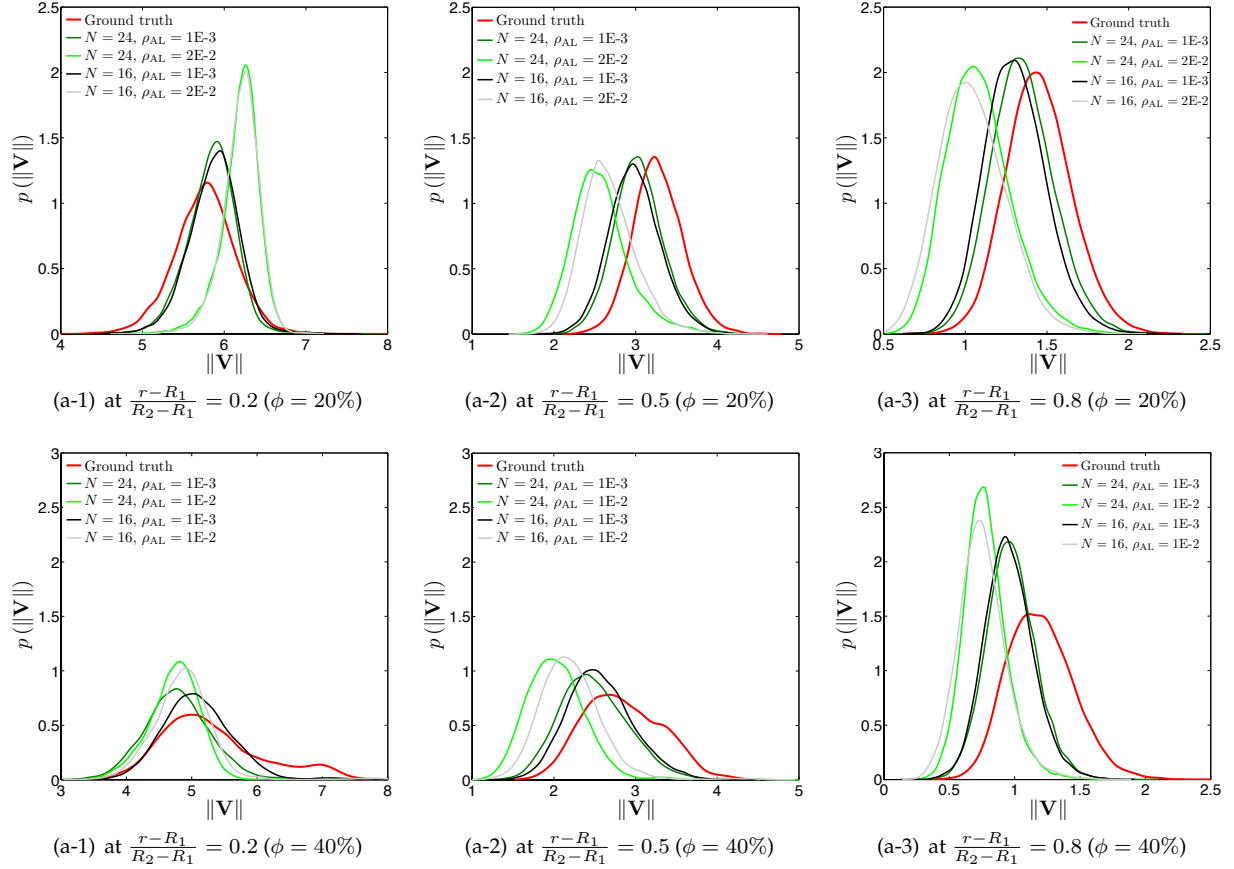


Figure 22: *Statistics of the velocity field of a Couette flow.* We compute the probability distribution function of the velocity magnitudes at points distributed equally in the azimuthal direction at three different radii. The top plots correspond to the volume fraction $\phi = 20\%$ and the bottom plots correspond to the volume fraction $\phi = 40\%$.

5. Conclusions

We have addressed issues with simulations of vesicle suspensions at low discretization resolutions. We have developed a robust method by introducing new schemes and implementing some standard techniques. An efficient scheme to determine an upsampling rate is used for computing the nonlinear terms without introducing spurious oscillations. A surface reparametrization algorithm smooths out vesicles' boundaries by penalizing their high-frequency components. The area and arc-length of the vesicles are corrected at each time step to allow for long-time scale simulations without changing the governing equations. A new reliable adaptive time-stepping scheme that works for all resolutions is used to choose the optimal time step size. Finally, a repulsion force between vesicles eliminates any chance of a non-physical collision. All these algorithms require certain parameters, and these were set by examining and minimizing the effect of each algorithm on the underlying physics.

We have discussed new error measures and performed a systematic error analysis to investigate the accuracy of our low-resolution simulations. The low-resolution correction algorithms we have presented are essential for stable simulations. Furthermore, by using these algorithms we are able to accurately capture the statistics of the underlying flow accurately with a coarse discretization. One of the most impressive examples is the Couette flow. Its low-resolution simulation, which takes less than a week, estimates accurately the upscaled quantities such as effective viscosity and statistics computed by the high-fidelity simulation, which takes more than a month.

Acknowledgements

This material is based upon work supported by AFOSR grants FA9550-12-10484; by NSF grant CCF-1337393; by the U.S. Department of Energy, Office of Science, Office of Advanced Scientific Computing Research, Applied Mathematics program under Award Numbers DE-SC0010518 and DE-SC0009286; by NIH grant 10042242; by DARPA grant W911NF-115-2-0121; and by the Technische Universität München—Institute for Advanced Study, funded by the German Excellence Initiative (and the European Union Seventh Framework Programme under grant agreement 291763). Any opinions, findings, and conclusions or recommendations expressed herein are those of the authors and do not necessarily reflect the views of the AFOSR, DOE, NIH, DARPA, and NSF. Computing time on the Texas Advanced Computing Centers Stampede system was provided by an allocation from TACC and the NSF.

References

- [1] S. Aland, S. Egerer, J. Lowengrub, and A. Voigt. Diffuse interface models of locally inextensible vesicles in a viscous flow. *Journal of Computational Physics*, 277:32–47, 2014.
- [2] B. K. Alpert. Hybrid Gauss-trapezoidal quadrature rules. *SIAM Journal on Scientific Computing*, 20:1551–1584, 1999.
- [3] Othmane Aouane and Marine Thiebaud, Abdelilah Benyoussef, Christian Wagner, and Chaouqi Misbah. Vesicle dynamics in a confined Poiseuille flow: From steady state to chaos. *Physical Review E*, 90(3):033011, 2014.
- [4] U. M. Ascher, S. J. Ruuth, and B. T. R. Wetton. Implicit-explicit methods for time dependent partial differential equations. *SIAM Journal on Numerical Analysis*, 32:797–823, 1995.
- [5] G. R. Baker and M. J. Shelley. On the connection between thin vortex layers and vortex sheets. *Journal of Fluid Mechanics*, 215:161–194, 1990.
- [6] J. Beaucourt, F. Rioual, T. Séon, T. Biben, and C. Misbah. Steady to unsteady dynamics of a vesicle in a flow. *Physical Review Letter E*, 69(1), 2004.
- [7] Paul J. Besl and Neil D. McKay. A Method for Registration of 3-D Shapes. *IEEE Transactions on Pattern Analysis and Machine Intelligence*, 14:239–256, 1992.
- [8] T. Biben and C. Misbah. Tumbling of vesicles under shear flow within an advected-field approach. *Physical Review E*, 67:031908, 2003.
- [9] C. Canuto, M. Y. Hussaini, A. Quarteroni, and T. A. Zang. *Spectral Methods in Fluid Dynamics*. Springer-Verlag, Berlin, 1987.
- [10] E. C. Eckstein, D. G. Bailey, and A. H. Shapiro. Self-diffusion of particles in shear flow of suspension. *Journal of Fluid Mechanics*, 79:191, 1977.
- [11] Z-G. Feng and E.E. Michaelides. Hydrodynamic force on spheres in cylindrical and prismatic enclosures. *Int. J. Multiphase Flow*, 28:479–496, 2002.
- [12] Z-G. Feng and E.E. Michaelides. The immersed boundary-lattice Boltzmann method for solving fluid-particles interaction problems. *Journal of Computational Physics*, 195:602–628, 2004.
- [13] J. B. Freund and H. Zhao. *A high-resolution fast boundary-integral method for multiple blood cells*, chapter 3, pages 71–111. CRC Press, 2010.
- [14] Jonathan B. Freund and M. M. Orescanin. Cellular flow in a small blood vessel. *Journal of Fluid Mechanics*, 671:466–490, 2011.

- [15] G. Ghigliotti, A. Rahimian, G. Biros, and C. Misbah. Vesicle migration and spatial organization driven by flow line curvature. *Physical Review Letters*, 106:028101, 2011.
- [16] R. Glowinski, T.-W. Pan, T.I. Hesla, D.D. Joseph, and J. Periaux. A fictitious domain approach to the direct numerical simulation of incompressible viscous flow past moving rigid bodies: Application to particulate flow. *Journal of Computational Physics*, 169:363–426, 2001.
- [17] H. L. Goldsmith and R. Skalak. Hemodynamics. *Annual Reviews of Fluid Mechanics*, 7:213–247, 1975.
- [18] Ernest Hairer, Gerhard Wanner, and Syvert Paul Nørsett. *Solving Ordinary Differential Equations I: Nonstiff Problems*. Springer, 1993.
- [19] D. Harmon, E. Vouga, B. Smith, R. Tamstorf, and E. Grinspun. Asynchronous contact mechanics. *ACM Transactions on Graphics (TOG)*, 26, 2009.
- [20] Thomas Y. Hou, John S. Lowengrub, and Michael J. Shelley. Removing the stiffness from interfacial flows with surface tension. *Journal of Computational Physics*, 114:312–338, 1994.
- [21] Gokberk Kabacaoglu, Bryan Quaife, and George Biros. Quantification of mixing in vesicle suspensions using numerical simulations in two dimensions. *Physics of Fluids*, 29(2):021901, 2017.
- [22] V. Kantsler, E. Segre, and V. Steinberg. Dynamics of interacting vesicles and rheology of vesicle suspension in shear flow. *Europhys. Lett.*, 82:58005, 2008.
- [23] B. Kaoui, N. Tahiri, T. Biben, H. Ez-Zahraouy, A. Benyoussef, G. Biros, and C. Misbah. What Dictates Red Blood Cell Shapes and Dynamics in the Microvasculature? *Physical Review E*, pages 1–11, 2011.
- [24] Badr Kaoui, Ruben J. W. Jonk, and Jens Harting. Interplay between microdynamics and macrorheology in vesicle suspensions. *Soft Matter*, 10:4735–4742, 2014.
- [25] M. Kraus, W. Wintz, U. Seifert, and R. Lipowsky. Fluid Vesicles in Shear Flow. *Physical Review Letter*, 77(17):3685–3688, 1996.
- [26] A. G. Kravchenko and P. Moin. On the effect of numerical errors in large eddy simulations of turbulent flows. *Journal of Computational Physics*, 131:310–322, 1997.
- [27] Antonio Lamura and Gerhard Gompper. Dynamics and rheology of vesicle suspensions in wall-bounded shear flow. *Europhys. Lett.*, 102:28004, 2013.
- [28] D. Leighton and A. Acrivos. The shear-induced migration of particles in concentrated suspensions. *Journal of Fluid Mechanics*, 181:415–439, 1987.
- [29] Dhairya Malhotra, Abtin Rahimian, Denis Zorin, and George Biros. A parallel algorithm for long-timescale simulation of concentrated vesicle suspensions in three dimensions. 2017.
- [30] Gary Marple, Alex Barnett, Adrianna Gillman, and Shravan Veerapaneni. A fast algorithm for simulating multiphase flows through periodic geometries of arbitrary shape. *SIAM J. Sci. Comput.*, 38(5): B740–B772, 2016.
- [31] C. Misbah. Vacillating breathing and tumbling of vesicles under shear flow. *Physical Review Letters*, 96(2), 2006.
- [32] Kahtrin Müller, Dmitry A. Fedosov, and Gerhard Gompper. Margination of micro- and nano-particles in blood flow and its effect on drug deliver. *Scientific Reports*, 4:4871, 2014.
- [33] Vivek Narsimhan, Hong Zhao, and Eric S. G. Shaqfeh. Coarse-grained theory to predict the concentration distribution of red blood cells in wall-bounded couette flow at zero reynolds number. *Physics of Fluids*, 25:061901, 2013.

- [34] H. Noguchi and D. G. Gompper. Shape transitions of fluid vesicles and red blood cells in capillary flows. *Proceedings Of The National Academy Of Sciences Of The United States Of America*, 102:14159–14164, 2005.
- [35] S. A. Orszag. Numerical simulation of incompressible flows within simple boundaries: Accuracy. *Journal of Fluid Mechanics*, 49:75–112, 1971.
- [36] S. A. Orszag. Fourier series on spheres. *Monthly Weather Review*, 102:56–75, 1974.
- [37] T-W. Pan, L. Shi, and R. Glowinski. A DLM/FD/IB method for simulating cell/cell and cell/particle interaction in microchannels. *Chinese Annals of Mathematics, Series B*, 31B-6:975–990, 2010.
- [38] G. S. Patterson and S. A. Orszag. Spectral calculations of isotropic performance of a subgrid scale model can be improved by turbulence: Efficient removal of aliasing interactions. *Physics of Fluids A*, 14:2538–2541, 1974.
- [39] Thomas Podgorski, Natacha Callens, Christophe Minetti, Gwennou Coupier, Frank Dubois, and Chaouqi Misbah. Dynamics of vesicle suspensions in shear flow between walls. *Microgravity Sci. Technol.*, 23:263–270, 2011.
- [40] C. Pozrikidis. The Axisymmetric Deformation Of A Red Blood Cell In Uniaxial Straining Stokes Flow. *Journal of Fluid Mechanics*, 216:231–254, 1990.
- [41] C. Pozrikidis. *Boundary Integral and Singularity Methods for Linearized Viscous Flow*. Cambridge University Press, New York, NY, USA, 1992.
- [42] Bryan Quaife and George Biros. High-volume fraction simulations of two-dimensional vesicle suspensions. *Journal of Computational Physics*, 274:245–267, 2014.
- [43] Bryan Quaife and George Biros. High-order adaptive time stepping for vesicle suspensions with viscosity contrast. *Procedia IUTAM*, 16:89–98, 2015.
- [44] Bryan Quaife and George Biros. Adaptive time stepping for vesicle suspensions. *Journal of Computational Physics*, 306:478–499, 2016.
- [45] Abtin Rahimian, Shravan K. Veerapaneni, and George Biros. Dynamic simulation of locally inextensible vesicles suspended in an arbitrary two-dimensional domain, a boundary integral method. *Journal of Computational Physics*, 229:6466–6484, 2010.
- [46] Abtin Rahimian, Shravan K. Veerapaneni, Denis Zorin, and George Biros. Boundary integral method for the flow of vesicles with viscosity contrast in three dimensions. *Journal of Computational Physics*, 298:766–786, 2015.
- [47] E. Sackmann. Supported membranes: Scientific and practical applications. *Science*, 271:43–48, 1996.
- [48] U. Seifert. Configurations of fluid membranes and vesicles. *Advances in Physics*, 46:13–137, 1997.
- [49] S. K. Veerapaneni, D. Gueyffier, D. Zorin, and G. Biros. A boundary integral method for simulating the dynamics of inextensible vesicles suspended in a viscous fluid in 2D. *Journal of Computational Physics*, 228(7):2334–2353, 2009.
- [50] S. K. Veerapaneni, A. Rahimian, G. Biros, and D. Zorin. A fast algorithm for simulating vesicle flows in three dimensions. *Journal of Computational Physics*, 230:5610–5634, 2011.
- [51] Etienne Vouga, David Harmon, Rasmus Tamstorf, and Eitan Grinspun. Asynchronous variational contact mechanics. *Computer Methods in Applied Mechanics and Engineering*, 200:2181–2194, 2011.

- [52] H. Zhao and E. S. G. Shaqfeh. The dynamics of a vesicle in shear flow. Technical report, Stanford University, 2009.
- [53] Hong Zhao and Eric S. G. Shaqfeh. The shape stability of a lipid vesicle in a uniaxial extensional flow. *Journal of Fluid Mechanics*, 719:345–361, 2013.
- [54] Hong Zhao and Eric S. G. Shaqfeh. The dynamics of a non-dilute vesicle suspension in simple shear flow. *Journal of Fluid Mechanics*, 725:709–731, 2013.
- [55] Hong Zhao, Amir H.G. Isfahani, Luke N. Olson, and Jonathan B. Freund. A spectral boundary integral method for flowing blood cells. *Journal of Computational Physics*, 229:3726–3744, 2010.